TÉCNICO LISBOA

Aerodynamic Shape Optimization with the Adjoint Method

Francisco Xavier Moreira Huhn

Thesis to obtain the Master of Science Degree in

Aerospace Engineering

Supervisor: Prof. Luís Rego da Cunha de Eça

Examination Committee

Chairperson: Prof. Fernando José Parracho Lau
Supervisor: Prof. Luís Rego da Cunha de Eça
Member of the Committee: Prof. José Firmino Aguilar Madeira

November 2015

Acknowledgments

Firstly, I would like to thank my supervisor at Airbus, Joël Brezillon, without whom this work would not have been possible.

I would like to thank Prof. João Pimentel Nunes, the best teacher I've ever had. I feel incredibly fortunate to have been his student.

I would like to thank all my friends, who are too many to be listed here. I thank you for all your support and memories, which I will cherish for the rest of my life.

Finally, I would like to thank Garazi Gómez de Segura for always supporting and being there for me.

Resumo

A maior parte dos custos de uma companhia aérea provêm do consumo de combustível. Desta forma, é do interesse das companhias aéreas e portanto, dos fabricantes de aeronaves, que este seja minimizado, por exemplo, através de redução de arrasto, isto é, optimização aerodinâmica.

Actualmente, este trabalho é feito por engenheiros com anos de experiência, usando o seu extenso conhecimento em aerodinâmica de aeronaves. No entanto, este trabalho é feito manualmente e por tentativa e erro, que se torna particularmente desafiante para geometrias complexas e aerodinâmica complexa.

A disciplina de optimização aerodinâmica automática responde a este problema. É uma disciplina relativamente recente e promete bons resultados onde o conhecimento humano falha. Nomeadamente, optimização aerodinâmica de forma com o método adjunto oferece bastantes vantagens em relação a outras técnicas. Esta técnica, em conjunção com outras será estudada e aplicada à optimização de um perfil aerodinâmico transsónico e de um *winglet* de um avião longo curso da Airbus.

Palavras-chave: optimização aerodinâmica, método adjunto, forma de perfil aerodinâmico, winglet

Abstract

The biggest cost for airlines is due to fuel consumption. Therefore, it is of the interest of airlines that fuel consumption be minimized. This task is done by aircraft manufacturers, including Airbus, for example, by reducing drag.

Currently, this work is done by experienced engineers with years of experience, making use of their extensive knowledge in aircraft aerodynamics. Nevertheless, this work is done manually and by trial and error, which becomes particularly challenging for complex shapes and complex aerodynamics.

The subject of automatic aerodynamic optimization responds to this problem. It is a recent subject and promises good results where human insight fails. Namely, aerodynamic shape optimization with the adjoint method offers many advantages with respect to other techniques. This technique, in conjunction with others will be studied and applied to the optimization of a transonic airfoil and of a winglet for a long range airplane of Airbus.

Keywords: aerodynamic optimization, adjoint method, airfoil shape, winglet

Contents

List of Tables

List of Figures

Nomenclature

Greek symbols

α	Angle of attack.
δ_{ij}	Kronecker's delta.
γ	Specific heat ratio.
λ	Thermal conductivity coefficient.
μ	Molecular viscosity coefficient.
ρ	Density.
τ	Shear stress.

Roman symbols

C_d, C_D	Coefficient of drag.
C_f	Coefficient of friction.
C_l, C_L	Coefficient of lift.
C_m, C_M	Coefficient of pitching moment.
C_p	Coefficient of pressure.
c_p	Enthalpy specific heat.
c_v	Pressure specific heat.
$\mathbf{D}$	Design variables vector.
E	Total energy.
e	Internal energy.
M	Mach number.
p	Pressure.
Pr	Prandtl number.

$\mathbf{Q}$	Flowfield vector.
$\mathbf{R}$	Discretized Navier-Stokes equations.
$\vec{q}$	Heat flux.
R	Perfect gas constant.
Re	Reynolds number.
$\mathbf{S}$	Trace-less viscous strain-rate.
T	Temperature.
$\vec{u}$	Velocity vector.
$\mathbf{X}$	Computational mesh.

Subscripts

∞	Free-stream condition.
$\vec{n}$	Normal component.
ref	Reference condition.
t	Time variable.
x, y, z	Cartesian components.

Superscripts

*	Adjoint.
T	Transpose.

Glossary

CFD Computational Fluid Dynamics is a branch of fluid mechanics that uses numerical methods and algorithms to solve problems that involve fluid flows.

DOE Design of Experiments is a method for design space exploration.

FFD Far-Field Drag is a drag decomposition analysis obtained with a conservation law applied at the far-field.

HPC High Performance Computing is a computer with a high-level computational capacity compared to a general-purpose computer.

KKT Karush-Kuhn-Tucker conditions are first order necessary conditions for a solution in nonlinear programming to be optimal.

SDA Sensibility and dependency analysis is a technique for finding correlations between a database of inputs and corresponding outputs.

SLSQP Sequential Least-Squares Quadratic Programming is a gradient-based algorithm for solving non-linearly constrained optimization problems.

WORMS WORkflow Management System is a flexible automated optimization chain developed and used by Airbus.

Chapter 1

Introduction

1.1 Motivation

In 2014, the airline industry was estimated to spend 212 billion (US) dollars in jet fuel, corresponding to 29.7% of the total operating costs [1]. In order to better respond to the highly competitive air transport industry, airlines look for the best fuel efficient aircraft. Furthermore, as fuel consumption is reduced, carbon emissions are also reduced, which is essential to comply with new environmental regulations.

Fuel consumption reduction can be achieved by drag reduction. As an example, a reduction of 1% in total drag corresponds to about 900kg of fuel savings for a 11000km flight.

To reduce drag, aircraft components such as: lifting surfaces, pylon, nacelles, fuselage, etc. are aerodynamically optimized. Currently, this work is done by experienced engineers who make use of their extensive knowledge in aircraft aerodynamics. However, this optimization is done by trial and error, a method that becomes challenging for complex shapes.

Because of its reduced need of human insight, a solution to this problematic is the use of a fully automatic aerodynamic optimization chain.

1.2 Topic Overview

Automatic aerodynamic optimization means that the user doesn't interact with the optimization process. He is responsible for setting up the design space and optimization and CFD parameters, but the whole optimization is carried out automatically.

The optimizer evaluates many designs, attempting to minimize a given objective function. The way these designs are generated highly depends on the chosen algorithm(s) and even the same algorithm may produce different results, depending on how aerodynamic and optimization information, such as lift, drag or their gradients, are computed. Since these metrics are obtained with a CFD solver, which has a high computational cost, the selection of the optimization optimization strategy is of crucial importance to keep a low turnaround time.

A class of algorithms that are commonly used when dealing with many parameters are gradient-based algorithms. These determine the successive designs based on the gradient of the objective function with respect to the design variables. Yet, conventional methods of gradient computation such as finite differences are usually computationally expensive, since they require many CFD evaluations. Moreover, they present issues such as the value step size. The adjoint method presents itself as an answer to this problem, having several advantages over such conventional gradient computation methods.

An optimization of a transonic airfoil and of a long range aircraft winglet with a gradient-based algorithm, aided by the adjoint method for gradient computation will be studied.

1.3 Objectives

The objectives of this internship are to:

- Understand the adjoint optimization process
- Understand the procedure of industrial aerodynamic studies
- Optimize aerodynamic shapes in two and three dimensions
- Assess the performance of the adjoint optimization in aerodynamic optimization
- Verify if the adjoint optimization is well-suited for aerodynamic optimization
- Understand how the optimizer improves aerodynamic shapes
- Understand the aerodynamic influence of each parameter

1.4 Outline

This work is divided into four parts:

- Aerodynamic Shape Optimization Theory
- Analysis and Optimization Tools at Airbus
- Two-dimensional optimization: RAE2822 transonic airfoil
- Three-dimensional optimization: long range aircraft winglet redesign

In the first part, a detailed analysis on the theory of aerodynamic shape optimization is given. The second part presents and explains each individual tool of the optimization toolchain. The third part deals with a two-dimensional optimization problem, which also serves as a first example of a complete optimization process. Finally, the fourth part is dedicated to a three-dimensional real case of the winglet of a long range aircraft designed by Airbus.

Chapter 2

Aerodynamic Shape Optimization

This chapter serves as an introduction to the theory of aerodynamic shape optimization.

2.1 Aerodynamics

In this section, the aerodynamics equations and models are presented. It starts with the appropriate form of the Navier-Stokes equations, from which the Reynolds Averaged Navier-Stokes (RANS) equations are derived. The Spalart-Allmaras turbulence model, required in order to close the system of equations, is then described. Finally, the aerodynamic coefficients utilized to assess the aerodynamic performance are defined and explained.

2.1.1 Navier-Stokes Equations

The fundamental equations of aerodynamics are the Navier-Stokes equations. These correspond to balance equations, which arise from applying Newton's second law to fluid motion, together with the assumption that the stress in the fluid is the sum of a diffusing viscous term (proportional to the gradient of velocity) and a pressure term. The unsteady compressible Navier-Stokes equations written in conservative form are presented in Eq. (2.1), where ρ is the density, $\vec{u}$ is the velocity, δ_{ij} is the Kroenocker's delta, p is the pressure, τ_{ij} is the shear stress, $\vec{q}$ is the heat flux, $E \equiv e + \frac{u_k u_k}{2}$ is called the total energy and the indices i, j range from 1 to the number of spatial dimensions.

$$\frac{\partial \rho}{\partial t} + \frac{\partial}{\partial x_j}\left(\rho u_j\right) = 0 \tag{2.1a}$$

$$\frac{\partial}{\partial t}\left(\rho u_i\right) + \frac{\partial}{\partial x_j}\left(\rho u_i u_j + p\delta_{ij} - \tau_{ji}\right) = 0 \tag{2.1b}$$

$$\frac{\partial}{\partial t}\left(\rho E\right) + \frac{\partial}{\partial x_j}\left(\rho u_j E + u_j p + q_j - u_i \tau_{ij}\right) = 0 \tag{2.1c}$$

For a Newtonian fluid and assuming Stokes Law for mono-atomic gases, both valid for air, the viscous stress is given by Eq. (2.2), where μ is the fluid's molecular viscosity coefficient and S^*_{ij} is the trace-less viscous strain-rate defined in Eq. (2.3).

$$\tau_{ij} = 2\mu S^*_{ij} \tag{2.2}$$

$$S^*_{ij} \equiv \frac{1}{2}\left(\frac{\partial u_i}{\partial x_j} + \frac{\partial u_j}{\partial x_i}\right) - \frac{1}{3}\frac{\partial u_k}{\partial x_k}\delta_{ij} \tag{2.3}$$

The heat flux q_j is given by Fourier's law Eq. (2.4), with T the temperature, c_p the enthalpy specific heat. The definition of Prandtl number - Eq. (2.5) - is used, where λ is the thermal conductivity coefficient.

$$q_j = -\lambda\frac{\partial T}{\partial x_j} \equiv -c_p\frac{\mu}{Pr}\frac{\partial T}{\partial x_j} \tag{2.4}$$

$$Pr \equiv \frac{c_p\mu}{\lambda} \tag{2.5}$$

Finally, this system of equations must be closed by an equation of state. Assuming a calorically perfect gas, the relations in Eq. (2.6) are valid. c_v is the pressure specific heat, R is the perfect gas constant

$$\gamma \equiv \frac{c_p}{c_v} \qquad p = \rho RT \qquad e = c_v T \qquad c_p - c_v = R \tag{2.6}$$

Equations (2.1)-(2.6), supplemented with gas data for γ, Pr, μ, R form a closed set of partial differential equations and need only be complemented with boundary conditions.

2.1.2 Reynolds Averaged Navier-Stokes Equations (RANS)

We will transform Eq. (2.1b) into dimensionless form. We start by defining reference variable values: U_{ref} reference speed, L_{ref} reference length, $\tau_{ref} = \frac{L_{ref}}{U_{ref}}$ reference time interval, ρ_{ref} reference density and μ_{ref} reference kinematic viscosity, from which we derive the normalized relations (2.7).

$$\begin{cases} t = \tau_{ref}\overline{t} & \Rightarrow \quad \dfrac{\partial}{\partial t} = \dfrac{L_{ref}}{U_{ref}}\dfrac{\partial}{\partial \overline{t}} \\ x_i = L_{ref}\overline{x}_i & \Rightarrow \quad \dfrac{\partial}{\partial x_i} = \dfrac{1}{L_{ref}}\dfrac{\partial}{\partial \overline{x}_i} \\ u_i = U_{ref}\overline{u}_i & \\ \rho = \rho_{ref}\overline{\rho} & \\ \mu = \mu_{ref}\overline{\mu} & \end{cases} \tag{2.7}$$

We introduce Eq. (2.7) into Eq. (2.1b) and we obtain Eq. (2.8), where Re is called the Reynolds number defined in Eq. (2.9).

$$\begin{aligned}\frac{\partial}{\partial \bar{t}}\left(\overline{\rho u}_i\right)+\frac{\partial}{\partial \overline{x}_j}\left(\overline{\rho u}_i\overline{u}_j+\frac{1}{2}\frac{p}{\frac{\rho_{ref}U_{ref}^2}{2}}\delta_{ij}\right) &= \frac{\mu_{ref}}{\rho_{ref}U_{ref}L_{ref}}\frac{\partial}{\partial \overline{x}_j}\left\{\overline{\mu}\left[\left(\frac{\partial \overline{u}_i}{\partial \overline{x}_j}+\frac{\partial \overline{u}_j}{\partial \overline{x}_i}\right)-\frac{2}{3}\frac{\partial \overline{u}_k}{\partial \overline{x}_k}\delta_{ij}\right]\right\} \\ &= \frac{1}{Re}\frac{\partial}{\partial \overline{x}_j}\left\{\overline{\mu}\left[\left(\frac{\partial \overline{u}_i}{\partial \overline{x}_j}+\frac{\partial \overline{u}_j}{\partial \overline{x}_i}\right)-\frac{2}{3}\frac{\partial \overline{u}_k}{\partial \overline{x}_k}\delta_{ij}\right]\right\}\end{aligned} \tag{2.8}$$

$$Re \equiv \frac{\rho_{ref}L_{ref}U_{ref}}{\mu_{ref}} \tag{2.9}$$

ρ_{ref}, U_{ref} and μ_{ref} are usually taken at infinity (unperturbed field) and L_{ref} is often the airfoil/wing (possibly mean aerodynamic) chord. The Reynolds number represents a ratio between inertial forces and viscous forces. When this number is low, viscous forces dominate. Conversely, when this number is high, inertial forces dominate. At low Reynolds number, the non-linear (convective) terms are small compared to the viscous terms, yielding a laminar flow. However, in the aviation industry $Re \sim 10^6$, meaning the non-linearities become important with respect to the viscous forces, rendering the flow chaotic. These phenomena take place at different time and length scales. If all scales are solved, the technique is called Direct Numerical Simulation. If only the largest scales are solved and the smallest are modeled, the technique is called Large Eddy Simulation. However, both of these techniques are computationally expensive. Finally, if all scales are modeled, the Reynolds Averaged Navier-Stokes equations are solved. These are derived by introducing the Reynolds decomposition (2.10) into the Navier-Stokes equations (2.1).

$$\underbrace{\phi(t,\vec{x})}_{\text{instantaneous}} = \underbrace{\overline{\phi}(\vec{x})}_{\text{average}} + \underbrace{\phi'(t,\vec{x})}_{\text{fluctuation}}, \qquad \overline{\phi}(\vec{x}) = \frac{1}{t}\int_{\tau}^{\tau+t}\phi(\xi,\vec{x})d\xi \tag{2.10}$$

2.1.3 Compressible Reynolds Averaged Navier-Stokes Equations

The Reynolds decomposition is usually used for averaging the Navier-Stokes equations in incompressible flow. For compressible flow, another decomposition called the Favre decomposition (2.11) is used.

$$\underbrace{\phi(t)}_{\text{instantaneous}} = \underbrace{\widetilde{\phi}}_{\text{average w.r.t. time}} + \underbrace{\phi''(t)}_{\text{fluctuation}}, \qquad \widetilde{\phi} = \frac{\overline{\rho\phi}}{\overline{\rho}} \tag{2.11}$$

Introducing Eq. (2.11) into the Navier-Stokes equations (2.1) and with certain hypothesis and modeling, we obtain Eq. (2.12), where μ_t, k, Pr_t are calculated with a turbulence model and μ, γ, Pr are obtained from gas data. These are a closed set of partial differential equations, which can be solved numerically.

$$\frac{\partial \overline{\rho}}{\partial t}+\frac{\partial}{\partial x_j}\left(\overline{\rho}\widetilde{u_j}\right)=0 \tag{2.12a}$$

$$\frac{\partial}{\partial t}\left(\overline{\rho}\widetilde{u_i}\right)+\frac{\partial}{\partial x_j}\left(\overline{\rho}\widetilde{u_i}\widetilde{u_j}+\overline{p}\delta_{ij}-\widetilde{\tau_{ji}^{tot}}\right)=0 \tag{2.12b}$$

$$\frac{\partial}{\partial t}\left(\overline{\rho}\widetilde{E}\right)+\frac{\partial}{\partial x_j}\left(\overline{\rho}\widetilde{u_j}\widetilde{E}+\widetilde{u_j}\overline{p}+\widetilde{q_j^{tot}}-\widetilde{u_i}\widetilde{\tau_{ij}^{tot}}\right)=0 \tag{2.12c}$$

$$\widetilde{\tau_{ij}^{tot}}\equiv\widetilde{\tau_{ij}^{lam}}+\widetilde{\tau_{ij}^{turb}}$$

$$\widetilde{\tau_{ij}^{lam}}\equiv\widetilde{\tau_{ij}}=\mu\left(\frac{\partial\widetilde{u_i}}{\partial x_j}+\frac{\partial\widetilde{u_j}}{\partial x_i}-\frac{2}{3}\frac{\partial\widetilde{u_k}}{\partial x_k}\delta_{ij}\right)$$

$$\widetilde{\tau_{ij}^{turb}}\equiv-\overline{\rho u_i''u_j''}\approx\mu_t\left(\frac{\partial\widetilde{u_i}}{\partial x_j}+\frac{\partial\widetilde{u_j}}{\partial x_i}-\frac{2}{3}\frac{\partial\widetilde{u_k}}{\partial x_k}\delta_{ij}\right)-\frac{2}{3}\overline{\rho}k\delta_{ij}$$

$$\widetilde{q_j^{tot}}=\widetilde{q_j^{lam}}+\widetilde{q_j^{turb}}$$

$$\widetilde{q_j^{lam}}\equiv\widetilde{q_j}\approx-c_p\frac{\mu}{Pr}\frac{\partial\widetilde{T}}{\partial x_j}=-\frac{\gamma}{\gamma-1}\frac{\mu}{Pr}\frac{\partial}{\partial x_j}\left(\frac{\overline{p}}{\overline{\rho}}\right)$$

$$\widetilde{q_j^{turb}}\equiv c_p\overline{\rho u_j''T}\approx-c_p\frac{\mu_t}{Pr_t}\frac{\partial\widetilde{T}}{\partial x_j}=-\frac{\gamma}{\gamma-1}\frac{\mu_t}{Pr_t}\frac{\partial}{\partial x_j}\left(\frac{\overline{p}}{\overline{\rho}}\right)$$

$$\overline{p}=(\gamma-1)\,\overline{\rho}\left(\widetilde{E}-\frac{\widetilde{u_k}\widetilde{u_k}}{2}-k\right)$$

2.1.4 Spalart-Allmaras Turbulence Model

The Spalart-Allmaras turbulence model is a one-equation model, which solves a transport equation for a viscosity variable $\widetilde{\nu}$, usually referred to as the Spalart-Allmaras variable, from which the turbulent eddy viscosity μ_t used in Eq. (2.12) is calculated. The complete description of the model is given in [19] and its compressible form in [20].

2.1.5 Aerodynamic Dimensionless Coefficients

2.1.5.1 Pressure Coefficient

The pressure coefficient (2.13) is the difference between local static pressure p and freestream static pressure p_∞, nondimensionalized by the freestream dynamic pressure $\frac{1}{2}\rho_\infty U_\infty^2$.

$$C_p\equiv\frac{p-p_\infty}{\frac{1}{2}\rho_\infty U_\infty^2} \tag{2.13}$$

2.1.5.2 Friction Coefficient

The friction coefficient (2.14) is the local wall shear stress τ_w, nondimensionalized by the freestream dynamic pressure.

$$C_f\equiv\frac{\tau_w}{\frac{1}{2}\rho_\infty U_\infty^2} \tag{2.14}$$

2.1.5.3 Drag Coefficient

Drag D is defined as the force parallel to the freestream velocity $\vec{U}_\infty$, which nondimensionalized by the freestream dynamic pressure times a reference surface area S_{ref} yields the drag coefficient Eq. (2.15).

$$C_D \equiv \frac{D}{\frac{1}{2}\rho_\infty U_\infty^2 S_{ref}} \tag{2.15}$$

The importance of the C_D can be justified by analyzing Breguet's range formula (2.16) for a jet aircraft. In Eq. (2.16), SFC is the specific fuel consumption, ρ is the air density, S is the reference surface and W_{initial} and W_{final} are the mission's initial and final weights, respectively. Therefore, if optimizing for range, it is logical that the drag be used as/or in the objective function in an aerodynamic shape optimization problem.

$$\text{Range} = \frac{2}{SFC}\sqrt{\frac{2}{\rho S}\frac{C_L}{C_D^2}}\left(\sqrt{W_{\text{initial}}} - \sqrt{W_{\text{final}}}\right) \tag{2.16}$$

There are two methods for calculating drag: near-field approach and far-field approach.

Near-Field Drag

The near-field approach consists in integrating the surface forces acting on the body and taking the component parallel to the freestream velocity of the resulting force. In Eq. (2.17), the integral represents the sum of all forces: pressure and friction. The dot product gives the component parallel to the freestream velocity $\vec{U}_\infty$, since the x axis is aligned with the freestream flow.

$$\begin{aligned} D &= \left\{\int_{S_B} \left[(p - p_\infty)\,\vec{n} + \vec{\tau}_w\right] dS\right\} \cdot \vec{e}_x \\ &= \int_{S_B} (p - p_\infty)\,\vec{n} \cdot \vec{e}_x dS + \int_{S_B} \vec{\tau}_w \cdot \vec{e}_x dS \\ &= \int_{S_B} (p - p_\infty)\, n_x dS + \int_{S_B} (\vec{\tau}_w)_x\, dS \\ &= D_p + D_f \end{aligned} \tag{2.17}$$

Far-Field Drag

There exist multiple formulations for the far-field drag analysis. Nevertheless, all of them are based on the law of conservation of momentum. We present a summary of the approach by Destarac and van der Vooren [22], which corresponds to the one implemented in the tool utilized later.

The theory is based on the assumption that the production of viscous drag and wave drag is confined to finite non-overlapping control volumes V_V (boundary and viscous shear layers) and V_W (shock layers) and that outside these volumes the flow can be considered to be inviscid. Eq. (2.18) expresses the total drag D as the sum of viscous drag D_v $(= D_{vp} + D_f)$, wave drag D_w and induced drag D_i.

$$D = \underbrace{D_p + D_f}_{\text{near-field drag}} = \underbrace{D_v + D_w + D_i}_{\text{far-field drag}} \tag{2.18}$$

However, because spurious viscous or wave drag can be generated in $V_{sp} \equiv V \setminus (V_V + V_W)$ by the numerical scheme used to solve the equations, outside the volumes V_V and V_W where viscous or wave drag production is physically justified, the near-field/far-field balance becomes Eq. (2.19), where $\vec{f}_{vw}$ is given by Eq. (2.20a) and $\vec{f_i}$ by Eq. (2.20b).

$$\begin{aligned} D &= D_p + D_f = D_v + D_w + D_{sp} + D_i \\ &= \underbrace{\int_{V_V} \nabla \cdot \vec{f}_{vw} dV}_{D_v} + \underbrace{\int_{V_W} \nabla \cdot \vec{f}_{vw} dV}_{D_w} \\ &+ \underbrace{\int_{V_{sp}} \nabla \cdot \vec{f}_{vw} dV}_{D_{sp}} + \underbrace{\int_{V} \nabla \cdot \vec{f_i} dV + D_f + D_p}_{D_i} \end{aligned} \tag{2.19}$$

$$\vec{f}_{vw} = -\rho\, \Delta\overline{u}\, \vec{U} + \vec{\tau}_x \tag{2.20a}$$

$$\vec{f_i} = -\rho(u - u_\infty - \Delta\overline{u})\vec{U} - (p - p_\infty)\vec{e}_x \tag{2.20b}$$

$$\Delta\overline{u} = u_\infty \sqrt{1 + 2\frac{\Delta H}{u_\infty^2} - \frac{2}{(\gamma - 1)M_\infty^2}\left[\left(e^{\frac{\delta s}{R}}\right)^{\frac{\gamma-1}{\gamma}} - 1\right]} - u_\infty \tag{2.20c}$$

2.1.5.4 Lift Coefficient

Lift L is defined as the force perpendicular to the freestream velocity $\vec{U}_\infty$, which nondimensionalized by the freestream dynamic pressure times a reference surface area S_{ref} yields the lift coefficient Eq. (2.21).

$$C_L \equiv \frac{L}{\frac{1}{2}\rho_\infty U_\infty^2 S_{ref}} \tag{2.21}$$

Similarly to the drag coefficient, the lift coefficient can be calculated by integrating the surface forces acting on the body and taking the component perpendicular to the freestream velocity of the resulting force. However, in contrast with the drag, the viscous lift component is negligible.

$$\begin{aligned} L &= \left\{\int_{S_B} \left[(p - p_\infty)\,\vec{n} + \vec{\tau}_w\right] dS\right\} \cdot \vec{e}_z \\ &= \int_{S_B} (p - p_\infty)\,\vec{n} \cdot \vec{e}_z dS + \int_{S_B} \vec{\tau}_w \cdot \vec{e}_z dS \\ &= \int_{S_B} (p - p_\infty)\, n_z dS + \int_{S_B} \tau_{w\,z} dS \\ &= L_p + L_f \\ &\approx L_p \end{aligned} \tag{2.22}$$

2.1.5.5 Pitching Moment Coefficient

The component of the resulting moment with respect to some point, parallel to $\vec{e}_y$ is called the pitching moment M. In a similar way to the previous aerodynamic coefficients, the pitching moment coefficient is defined in Eq. (2.23), where L_{ref} is a reference length, usually the (possibly mean aerodynamic) chord. The pitching moment is considered positive when it acts to pitch the airfoil/wing nose-up. It is usually of importance, either because an increase must be compensated by the elevator/canard, which might be penalizing in terms of aerodynamics; or because of structural aspects such as twisting moment.

$$C_m \equiv \frac{M}{\frac{1}{2}\rho_\infty U_\infty^2 S_{ref} L_{ref}} \tag{2.23}$$

2.2 Shape

In aerodynamic shape optimization, only design variables which modify the shape of the body are considered. This means that variables such as Mach number, Reynolds number, etc. are fixed during optimization.

The set of design variables $\mathbf{D}$ describes the surface of the body. The original mesh is then deformed at the surface from the original shape to the new shape. This deformation is then propagated to the rest of mesh volume. We define $\mathbf{X}_s$ as the set of mesh surface nodes, from which $\mathbf{X}_s = \mathbf{X}_s(\mathbf{D})$. Furthermore, we define $\mathbf{X}$ as the set of all mesh nodes, including surface nodes $\mathbf{X}_s \subset \mathbf{X}$.

2.3 Optimization

2.3.1 Problem Definition

Consider the vector of design variables $\mathbf{D}$, computational mesh $\mathbf{X}$, flowfield variables $\mathbf{Q}$ and a cost function $f = f(\mathbf{Q}, \mathbf{X})$. Furthermore consider a set of equality constraints $\mathbf{G} = 0$ and a set of inequality constraints $\mathbf{H} \leq 0$. Then, the aerodynamic optimization problem is defined by Eq. (2.24).

$$\begin{aligned} \underset{\mathbf{D}}{\text{minimize}} \quad & f(\mathbf{Q}, \mathbf{X}) \\ \text{subject to} \quad & \mathbf{G}(\mathbf{Q}, \mathbf{X}) \leq 0 \\ & \mathbf{H}(\mathbf{Q}, \mathbf{X}) = 0 \end{aligned} \tag{2.24}$$

Optimization algorithms for solving problems such as Eq. (2.24) are divided into gradient-based and non gradient-based algorithms. Genetic algorithms are found in the latter. In such an algorithm, a population of candidate designs is evolved toward better solutions, through an iterative process, with the population in each iteration called a generation. The algorithm terminates when either a maximum number of generations has been produced, or a satisfactory fitness (cost function) level has been reached for the population. However, genetic algorithms do not scale well: as the number of elements subject to mutation increases, the size of the corresponding design space increases exponentially. Thus, for aerodynamic optimization, where the number of design variables ranges from tens to hundreds, these methods are not well suited.

2.3.2 Gradient-based optimization

The fundamental information in all gradient-based algorithms is the sensitivity or gradient of the cost function f with respect to the design variables $\mathbf{D}$.

$$\nabla f = \frac{df}{d\mathbf{D}} = \left[\frac{\partial f}{\partial \mathbf{D}_i}\right], \quad i = 1, \ldots, |\mathbf{D}| \tag{2.25}$$

Based on this gradient, the optimizer (optimization algorithm) decides where to go to in the design space. As an example, a generic gradient-descending method computes the next design variables values $\mathbf{D}^{k+1}$ at iteration k in the following way, where γ is algorithm-dependent, possibly constant:

$$\mathbf{D}^{k+1} = \mathbf{D}^k - \gamma \left.\frac{df}{d\mathbf{D}}\right|_{\mathbf{D}=\mathbf{D}^k}$$

Moreover, in an unconstrained optimization, a necessary condition for a minima is the nullity of Eq. (2.25). The more general KKT condition, used in constrained optimization problems such as Eq. (2.24) and presented in Section 2.3.2.3, also makes use of this gradient. Therefore, precision and speed of computation of this gradient are of paramount importance for the whole optimization process.

2.3.2.1 Gradient computation by finite differences

The gradient (2.25) can be computed by forward Eq. (2.26a) or backward Eq. (2.26b) finite differences, which are first-order methods.

$$\frac{df}{d\mathbf{D}} = \frac{f(\mathbf{D}+\Delta\mathbf{D}) - f(\mathbf{D})}{\Delta\mathbf{D}} + O(\Delta\mathbf{D}) \tag{2.26a}$$

$$\frac{df}{d\mathbf{D}} = \frac{f(\mathbf{D}) - f(\mathbf{D}-\Delta\mathbf{D})}{\Delta\mathbf{D}} + O(\Delta\mathbf{D}) \tag{2.26b}$$

Summing Eq. (2.26a) and Eq. (2.26b), we obtain the centered finite difference Eq. (2.27), which is a second-order method.

$$\frac{df}{d\mathbf{D}} = \frac{f(\mathbf{D}+\Delta\mathbf{D}) - f(\mathbf{D}-\Delta\mathbf{D})}{2\Delta\mathbf{D}} + O(\Delta\mathbf{D}^2) \tag{2.27}$$

Therefore, the computation of the gradient Eq. (2.25) requires $|\mathbf{D}|+1$ flow solutions (CFD evaluation) for the first-order methods - one $f(\mathbf{D}+\Delta\mathbf{D})$ for each $\Delta\mathbf{D}$ in the direction of each design variable plus $f(\mathbf{D})$. Similarly $2\,|\mathbf{D}|$ flow solutions are required for the second-order method.

In both cases, the cost of gradient computation is directly proportional to the number of design variables $|\mathbf{D}|$. For aerodynamic optimization, this number ranges from tens to hundreds, rendering these methods prohibitively expensive. Furthermore, knowing which value of finite differences step $\Delta\mathbf{D}$ to use is not trivial. The error of gradient computation by finite differences as a function of the step $\Delta\mathbf{D}$ is shown in Fig. 2.1. For small $\Delta\mathbf{D}$, numerical errors are dominant due to the numeric subtraction in the dividend. In fact, as $\Delta\mathbf{D}$ grows smaller, the difference between $f(\mathbf{D}+\Delta\mathbf{D})$ and $f(\mathbf{D}-\Delta\mathbf{D})$ becomes smaller, canceling out the most significant and least erroneous digits and making the most erroneous digits more important. Beyond a certain $\Delta\mathbf{D}$, as its value grows, the error $O(\Delta\mathbf{D}^2)$ also grows.

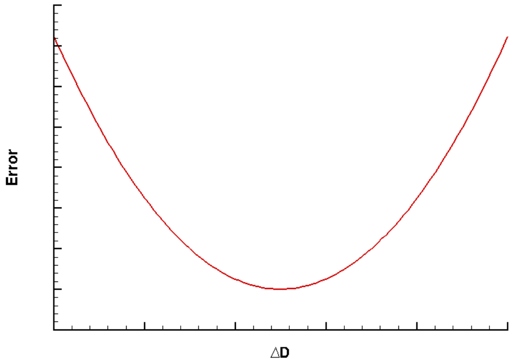

Figure 2.1: Gradient computation error vs Gradient step size $\Delta\mathbf{D}$

2.3.2.2 Gradient computation by the adjoint method

Consider the vector of discretized residual equations for the Navier-Stokes equations $\mathbf{R} = \mathbf{R}(\mathbf{Q}, \mathbf{X})$ and its steady-state solution of the form $\mathbf{R}(\mathbf{Q}, \mathbf{X}) = 0$. We define a Lagrangian function $\mathcal{L}$, given by Eq. (2.28), where $\mathbf{\Lambda}$ represents a vector of Lagrange multipliers, or adjoint variables.

$$\mathcal{L}(\mathbf{Q}, \mathbf{X}, \mathbf{\Lambda}) = f(\mathbf{Q}, \mathbf{X}) + \mathbf{\Lambda}^T \mathbf{R}(\mathbf{Q}, \mathbf{X}) \tag{2.28}$$

Because $\mathbf{R}(\mathbf{Q}, \mathbf{X}) = 0$, we have

$$\frac{d\mathcal{L}}{d\mathbf{D}} = \frac{df}{d\mathbf{D}}$$

meaning that if we compute the gradient $\frac{d\mathcal{L}}{d\mathbf{D}}$, we also compute the gradient $\frac{df}{d\mathbf{D}}$ needed for the gradient-based optimization algorithm.

Differentiating Eq. (2.28) with respect to $\mathbf{D}$ and rearranging terms yields Eq. (2.29).

$$\begin{aligned}
\frac{d\mathcal{L}}{d\mathbf{D}} &= \frac{df}{d\mathbf{D}} && + \mathbf{\Lambda}^T \frac{d\mathbf{R}}{d\mathbf{D}} \\
&= \left[\left(\frac{\partial \mathbf{Q}}{\partial \mathbf{D}}\right)^T \frac{\partial f}{\partial \mathbf{Q}} + \left(\frac{\partial \mathbf{X}}{\partial \mathbf{D}}\right)^T \frac{\partial f}{\partial \mathbf{X}} \right] && + \left[\left(\frac{\partial \mathbf{Q}}{\partial \mathbf{D}}\right)^T \frac{\partial \mathbf{R}}{\partial \mathbf{Q}} + \left(\frac{\partial \mathbf{X}}{\partial \mathbf{D}}\right)^T \frac{\partial \mathbf{R}}{\partial \mathbf{X}} \right] \mathbf{\Lambda} \\
&= \left(\frac{\partial \mathbf{X}}{\partial \mathbf{D}}\right)^T \left[\frac{\partial f}{\partial \mathbf{X}} + \left(\frac{\partial \mathbf{R}}{\partial \mathbf{X}}\right)^T \mathbf{\Lambda} \right] && + \left(\frac{\partial \mathbf{Q}}{\partial \mathbf{D}}\right)^T \left[\frac{\partial f}{\partial \mathbf{Q}} + \left(\frac{\partial \mathbf{R}}{\partial \mathbf{Q}}\right)^T \mathbf{\Lambda} \right]
\end{aligned} \tag{2.29}$$

The term $\left(\frac{\partial \mathbf{Q}}{\partial \mathbf{D}}\right)^T$ is computationally expensive, since it requires a number of flow solutions proportional to $|\mathbf{D}|$, as in Section 2.3.2.1. However and since $\mathbf{\Lambda}$ is essentially arbitrary, the coefficient multiplying $\left(\frac{\partial \mathbf{Q}}{\partial \mathbf{D}}\right)^T$ can be eliminated with Eq. (2.30), called the *Adjoint System of Equations*.

$$\left(\frac{\partial \mathbf{R}}{\partial \mathbf{Q}}\right)^T \mathbf{\Lambda} = -\frac{\partial f}{\partial \mathbf{Q}} \tag{2.30}$$

The gradient $\frac{d\mathcal{L}}{d\mathbf{D}}$ is then given by Eq. (2.31).

$$\frac{d\mathcal{L}}{d\mathbf{D}} = \left(\frac{\partial \mathbf{X}}{\partial \mathbf{D}}\right)^T \left[\frac{\partial f}{\partial \mathbf{X}} + \left(\frac{\partial \mathbf{R}}{\partial \mathbf{X}}\right)^T \mathbf{\Lambda}\right] \tag{2.31}$$

The $\frac{\partial \mathbf{X}}{\partial \mathbf{D}}$ term represents the mesh sensitivity and is developed in Eq. (2.32). Because $\mathbf{X}_s$ is *analytically* defined by $\mathbf{D}$, finite differences are not required.

$$\frac{\partial \mathbf{X}}{\partial \mathbf{D}} = \frac{\partial \mathbf{X}}{\partial \mathbf{X}_s}\frac{\partial \mathbf{X}_s}{\partial \mathbf{D}} \tag{2.32}$$

Finally, inserting Eq. (2.32) into Eq. (2.31), we obtain Eq. (2.33), where Λ is obtained by solving Eq. (2.30).

$$\frac{d\mathcal{L}}{d\mathbf{D}} = \left(\frac{\partial \mathbf{X}_s}{\partial \mathbf{D}}\right)^T \left(\frac{\partial \mathbf{X}}{\partial \mathbf{X}_s}\right)^T \left[\frac{\partial f}{\partial \mathbf{X}} + \left(\frac{\partial \mathbf{R}}{\partial \mathbf{X}}\right)^T \mathbf{\Lambda}\right] \tag{2.33}$$

2.3.2.3 Karush–Kuhn–Tucker (KKT) conditions

The KKT conditions are first order necessary conditions for a solution in nonlinear programming to be optimal, provided that some regularity conditions are satisfied. They are a generalization of the method of Lagrange multipliers, which allows only equality constraints. Consider the optimization problem (2.34).

$$\begin{aligned} \underset{x}{\text{minimize}} \quad & f(x) \\ \text{subject to} \quad & \mathbf{G}(x) \leq 0 \\ & \mathbf{H}(x) = 0 \end{aligned} \tag{2.34}$$

If x_m is a local minimum, then the KKT conditions (2.35) must be verified.

$$-\nabla f(x_m) = \sum_{i=1}^{|\mathbf{G}|} \mu_i \nabla \mathbf{G}_i(x_m) + \sum_{j=1}^{|\mathbf{H}|} \lambda_j \nabla \mathbf{H}_j(x_m) \tag{2.35a}$$

$$\begin{cases} \mathbf{G}_i(x_m) \leq 0, & i = 1, \ldots, |\mathbf{G}| \\ \mathbf{H}_j(x_m) = 0, & j = 1, \ldots, |\mathbf{H}| \end{cases} \tag{2.35b}$$

$$\mu_i \geq 0, \qquad i = 1, \ldots, |\mathbf{G}| \tag{2.35c}$$

$$\mu_i \mathbf{G}_i(x_m) = 0, \qquad i = 1, \ldots, |\mathbf{G}| \tag{2.35d}$$

Notice that the inequality contribution $\mu_i \nabla \mathbf{G}_i(x_m)$ in Eq. (2.35a) only needs to be considered when $\mathbf{G}_i(x_m) = 0$, since if $\mathbf{G}_i(x_m) < 0$ and $\mu_i \geq 0$ (from Eq. (2.35c)), then $\mu_i = 0$ is necessary to satisfy Eq. (2.35d), rendering $\mu_i \nabla \mathbf{G}_i(x_m) = 0$. This applies for example to design space boundary constraints $x_i \in [l_i, u_i] \Leftrightarrow x_i - u_i \leq 0 \wedge l_i - x_i \leq 0$.

2.3.2.4 Sequential Least Squares Programming (SLSQP)

SLSQP stands for Sequential Least-Squares Quadratic Programming. It is a gradient-based algorithm for non-linearly constrained optimization problems, which supports both equality and inequality constraints. Consider the generic optimization problem (2.34).

The Lagrangian of the problem is given by Eq. (2.36), where μ and λ are the Lagrange multipliers.

$$\mathcal{L}(x, \mu, \lambda) = f(x) + \mu^T \mathbf{G}(x) + \lambda^T \mathbf{H}(x) \tag{2.36}$$

At iteration k, the algorithm defines an appropriate search direction d_k as a solution to the quadratic problem (2.37). The Hessian matrix $\nabla^2_{xx}\mathcal{L}$ is computed with a BFGS update. [18]

$$\begin{aligned} \underset{d}{\text{minimize}} \quad & f(x_k) + \nabla f(x_k)^T d + \tfrac{1}{2} d^T \nabla^2_{xx}\mathcal{L}(x_k, \mu_k, \lambda_k) d \\ \text{subject to} \quad & \mathbf{G}(x_k) + \nabla \mathbf{G}(x_k)^T d \leq 0 \\ & \mathbf{H}(x_k) + \nabla \mathbf{H}(x_k)^T d = 0 \end{aligned} \tag{2.37}$$

2.3.3 Design of Experiments (DOE)

Design of Experiments is a method for design space exploration. The way in which the space design is explored depends on the chosen sampling algorithm, of which there are many, such as:

- Random sampling
- Halton sampling
- Latin hypercube sampling
- Etc.

The chosen algorithm for this work is the *Latin hypercube sampling*, since the probability that the samples are clustered is low.

A square grid containing sample positions is a Latin square if and only if there is only one sample in each row and each column. Fig. 2.2a and Fig. 2.2b are examples of Latin squares, while Fig. 2.2c isn't. The generalization of a Latin square to an arbitrary number of dimensions is called a Latin hypercube.

Consider a design space of N dimensions and a sampling of M samples. Then, the range of each variable is divided into M equiprobable intervals. M sample points are then placed to satisfy the Latin hypercube requirements.

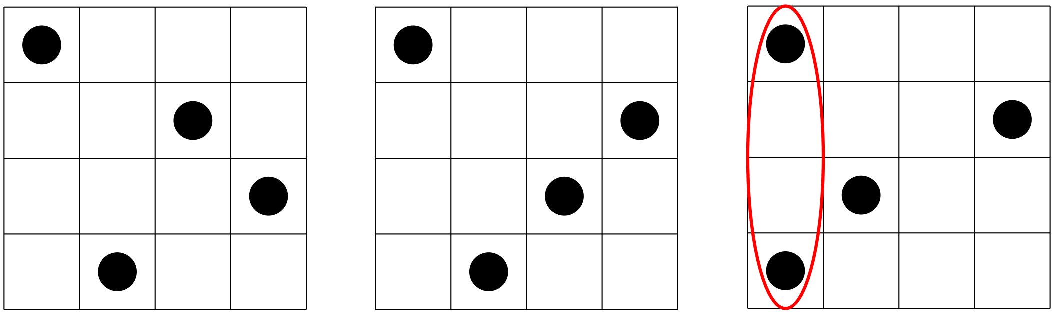

(a) Latin square

(b) Latin square

(c) Not Latin square

Figure 2.2: Square grid examples

Chapter 3

Analysis and Optimization Tools

In this chapter, the tools utilized for either analysis or optimization are presented. Furthermore, an explanation of how they work is given.

3.1 Computational Fluid Dynamics

3.1.1 Mesh

At Airbus, elsA only supports structured multi-block meshes. The meshes are generated using ANSYS ICEM software. The objective is to have high-quality meshes, which satisfy some mesh quality and boundary layer criteria (e.g. maximum skewness and $y^+_{\text{first cell}} \sim 1$, respectively).

Because the generated mesh is fine, CFD simulations take a long time to run. In order to speed up the process, the mesh is coarsed once or twice, corresponding to a reduction to one half or one quarter of the original points, respectively. These meshes are called ”medium” and ”coarse”, respectively, and they are used during the optimization process. After the optimization process finishes, the optimized solution is then validated using the original fine mesh.

3.1.2 Solver

The CFD solver used in this work is elsA. It is a finite-volume CFD solver developed by ONERA (and co-developed by many others) and it is one of the two *de facto* CFD solvers used in Airbus. elsA is capable of both external and internal complex flow simulations in aerodynamics and handles structured multi-block meshes. Its settings are divided into five groups: flight conditions, turbulence model, spatial integration, time integration, geometry parameters. Common settings to all CFD computations for this work are presented in Tbl. 3.1.

Simulation Type	Compressible RANS
Turbulence Model	Spalart-Allmaras
Spatial Int. Scheme	2nd order ROE
Limiter	Valbada

Table 3.1: Common elsA settings

3.2 WORMS Optimization Chain

WORMS stands for WORkflow Management System. It is a flexible automated optimization chain, which links all different components necessary to the optimization process. At each step the output of each component is validated and the input of a component is sourced from the output of one or multiple previous components.

WORMS allows both direct-mode (gradient by finite differences) and reverse-mode (gradient by solving the adjoint state) optimizations. The last four components described below and their chaining belong only to the reverse-mode optimization workflow.

3.2.1 Padge

Padge is responsible for the parameterization of the body surface. That is, for a given design variables vector $\mathbf{D}$, it is responsible for calculating the surface points:

$$(x, y, z)_s = \begin{cases} F(\mathbf{D}, u) & u \in [0,1] & \text{if 2D geometry} \\ F(\mathbf{D}, u, v) & u, v \in [0,1] & \text{if 3D geometry} \end{cases}$$

Given the new design vector variables vector $\mathbf{D}$, Padge computes the new surface mesh $\mathbf{X}_s$. Comparing this with the original surface mesh $\mathbf{X}_s^0$, the displacement of each surface mesh node is computed $\delta\mathbf{X}_s = \mathbf{X}_s - \mathbf{X}_s^0$.

Input	**Output**
Computational mesh $\mathbf{X}^0 \supset \mathbf{X}_s^0$	Surface mesh displacement $\delta\mathbf{X}_s$
Design variables vector $\mathbf{D}$	
Parameterization $\mathbf{F}(\mathbf{D}, u, v)$	

Table 3.2: Padge input/output summary

3.2.1.1 Shape Matching

Given a parameterization of the body surface, a set of design variable values $\mathbf{D} = \mathbf{D}_{\text{original}}$ must be found in order to match the original shape. The process of finding $\mathbf{D}$ is called *shape matching*. It is an iterative process and it converges when the mean distance between the initial shape and the parameterized shape is less than a defined error value, usually $1\,\text{mm}$ for a $1\,\text{m}$ chord.

3.2.1.2 CAD to Mesh Link

In order to be able to compute the displacement $\delta \mathbf{X}_s = \mathbf{X}_s - \mathbf{X}_s^0$, the location of each point $\left(\mathbf{X}_s^0\right)_i$ of the original surface mesh on the new surface mesh $\left(\mathbf{X}_s\right)_i$ must be known. This is done by finding a tuple $(u, v)_i = F^{-1}((\mathbf{X}_s^0)_i)$ for each mesh point of the original surface mesh and supplying it to new surface mapping $F(u, v) = F(\mathbf{D}, u, v)$.

3.2.2 VolDef

VolDef stands for Volume Deformation and it's responsible for mesh deformation. Given the surface mesh displacement $\delta \mathbf{X}_s$ calculated by Padge, the complete mesh $\mathbf{X}$ is deformed. This deformation is done by layers inside a cone emanating from the surface, with an exponential damping factor.

Input	Output
Computational mesh $\mathbf{X}^0 \supset \mathbf{X}_s^0$	New mesh $\mathbf{X}$
Surface mesh displacement $\delta \mathbf{X}_s$	

Table 3.3: VolDef input/output summary

3.2.3 elsA

elsA is the CFD solver utilized both for direct CFD simulations (e.g.: airfoil polar) and for optimizations. A description of its characteristics and capabilities is given in Section 3.1.2.

Input	Output
New mesh $\mathbf{X}$	Flow field $\mathbf{Q}$
	Residuals $\mathbf{R}$

Table 3.4: elsA input/output summary

3.2.3.1 Target Lift

For this work, all optimizations are run for a fixed target lift coefficient. This doesn't mean that optimization of a range of lift coefficients can not be done. It means that performances are always evaluated at the same fixed target lifts.

The target lift method works by changing the angle of attack until finding an angle of attack for which the lift coefficient is equal to the target lift coefficient. The changes in angle of attack follow an iterative algorithm Eq. (3.1), where ω is a damping parameter, usually 0.6 and $\frac{dC_L}{d\alpha}$ is supplied by the user, usually within the range $[0.10, 0.14]$.

$$\alpha_{n+1} = \alpha_n + \omega \left(\frac{dC_L}{d\alpha} \right)^{-1} \left((C_L)_{\text{target}} - C_L(\alpha_n) \right) \tag{3.1}$$

The simulation starts at a predefined α_0 for `Step Number` time steps. Then, the iterative algorithm begins and the flow is computed at each α_n for `NStepLoop` time steps. When $|(C_L)_{\text{target}} - C_L(\alpha_n)| \leq \epsilon$, where ϵ is a pre-defined tolerance, the iterative algorithm stops and the CFD simulation is run for a final `NStepEnds` time steps.

3.2.4 ZAPP/ZAPP-rev

ZAPP is a post-processing tool, responsible for computing the desired performance metrics f_i (e.g.: C_D, C_L, etc.) and its reverse mode computes their partial derivatives with respect to the mesh nodes $\frac{\partial f_i}{\partial \mathbf{X}}$ and with respect to the flow vector variables $\frac{\partial f_i}{\partial \mathbf{Q}}$.

Input	Output
New mesh $\mathbf{X}'$	Performance metrics f_i
Flow field $\mathbf{Q}$	Partial derivatives $\frac{\partial f_i}{\partial \mathbf{X}}, \frac{\partial f_i}{\partial \mathbf{Q}}$

Table 3.5: ZAPP input/output summary

3.2.5 elsA-reverse

elsA-reverse is responsible for solving the adjoint-state $\mathbf{\Lambda}$ as described in Section 2.3.2.2. The adjoint-state is then used to compute the full derivative of the function f_i with respect to the mesh nodes positions (3.2).

$$\frac{df_i}{d\mathbf{X}} = \frac{\partial f_i}{\partial \mathbf{X}} + \left(\frac{\partial \mathbf{R}}{\partial \mathbf{X}}\right)^T \mathbf{\Lambda} \tag{3.2}$$

Input	Output
New mesh $\mathbf{X}$	Adjoint state $\mathbf{\Lambda}$
Flow field $\mathbf{Q}$	
Residues $\mathbf{R}$	Full derivative $\frac{df_i}{d\mathbf{X}}$
Partial derivatives $\frac{\partial f_i}{\partial \mathbf{X}}, \frac{\partial f_i}{\partial \mathbf{Q}}$	

Table 3.6: elsA-reverse input/output summary

3.2.6 VolDef-reverse

VolDef-reverse computes the derivative of the functions f_i with respect to the surface mesh nodes. It computes the partial derivative $\frac{\partial \mathbf{X}_s}{\partial \mathbf{X}}$ and multiplies by the full derivative (3.2) computed by elsA-reverse, resulting in Eq. (3.3).

$$\frac{df_i}{d\mathbf{X}_s} = \left(\frac{\partial \mathbf{X}}{\partial \mathbf{X}_s}\right)^T \left[\frac{\partial f_i}{\partial \mathbf{X}_s} + \left(\frac{\partial \mathbf{R}}{\partial \mathbf{X}}\right)^T \mathbf{\Lambda}\right] \tag{3.3}$$

Input	**Output**
New mesh $\mathbf{X}$	Full derivative $\frac{df_i}{d\mathbf{X}_s}$
Full derivative $\frac{df_i}{d\mathbf{X}}$	

Table 3.7: VolDef-reverse input/output summary

3.2.7 Padge-reverse

Padge-reverse is responsible for the final step, which is transforming the derivative with respect to the surface mesh nodes, that is, the ”shape”, into a derivative with respect to the design variables. This is done by computing $\frac{\partial \mathbf{X}_s}{\partial \mathbf{D}}$ and multiplying by (3.3).

Input	**Output**
Parameterization $\mathbf{F}(\mathbf{D}, u, v)$	Full derivative $\frac{df_i}{d\mathbf{D}}$
Full derivative $\frac{df_i}{d\mathbf{X}_s}$	

Table 3.8: Padge-reverse input/output summary

3.2.8 Optimizer

The optimizer receives the gradient of the objective and constraint functions and decides the next set of design variable values $\mathbf{D}$. The complete workflow is described in Fig. 3.1.

3.3 Post-processing

3.3.1 KKT Optimization Analysis

As described in Section 2.3.2.3, the KKT conditions are necessary conditions for a local optimum. An analysis of the KKT conditions are done by an in-house software.

3.3.2 Flow visualization

In order to visualize the flow field and relevant aerodynamic data, an in-house software called QuickView was used. It supports 3D visualization and multiple types of plot and is highly customizable.

3.3.3 FFD Aerodynamic Analysis

As described in Section 2.1.5.3, drag can be decomposed with a far-field analysis. This is done with an in-house software called FFD72.

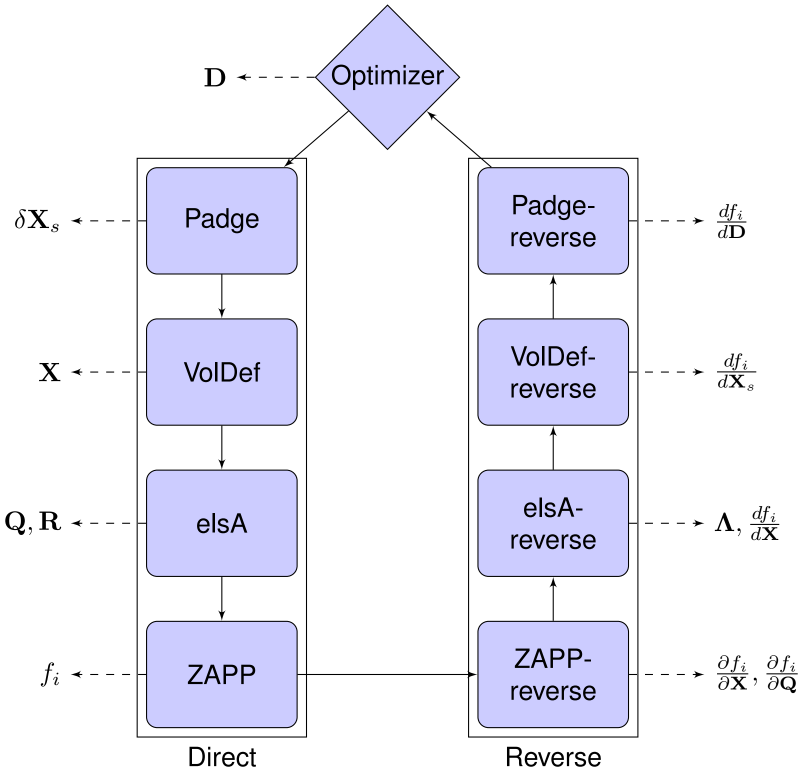
$\mathbf{D}$
Optimizer
$\delta\mathbf{X}_s$
Padge
Padge-reverse
$\frac{df_i}{d\mathbf{D}}$
$\mathbf{X}$
VolDef
VolDef-reverse
$\frac{df_i}{d\mathbf{X}_s}$
$\mathbf{Q}, \mathbf{R}$
elsA
elsA-reverse
$\mathbf{\Lambda}, \frac{df_i}{d\mathbf{X}}$
f_i
ZAPP
ZAPP-reverse
$\frac{\partial f_i}{\partial \mathbf{X}}, \frac{\partial f_i}{\partial \mathbf{Q}}$
Direct
Reverse

Figure 3.1: WORMS reverse-mode optimization workflow

Chapter 4

RAE2822 Airfoil Optimization

The RAE2822 airfoil is a transonic airfoil. It has been extensively studied both computationally and experimentally.

4.1 Test Case Definition

The flight conditions of the case are:

- $M = 0.73$
- $Re = 6.5 \times 10^6$

4.1.1 Mesh

The mesh was generated in ANSYS ICEM with the objective of having $y^+ \sim 0.3$ for the nearest mesh node to the wall. Then, this mesh was coarsed to a medium mesh. The objective is to run optimizations on the medium mesh (including reverse mode) and run the direct flow solutions of the initial and final shapes on the fine mesh in order to validate the optimizations results, as described in Section 3.1.1. The mesh is composed of two planes, in order to create the volume cells. A summary of the mesh characteristics (including the two planes) is given in Tbl. 4.1. Both complete and zoomed views of the mesh are in Fig. 4.1.

	Medium	Fine
Blocks	28	
Nodes	78736	306600
Surface Nodes	22188	86020

Table 4.1: RAE2822 mesh summary

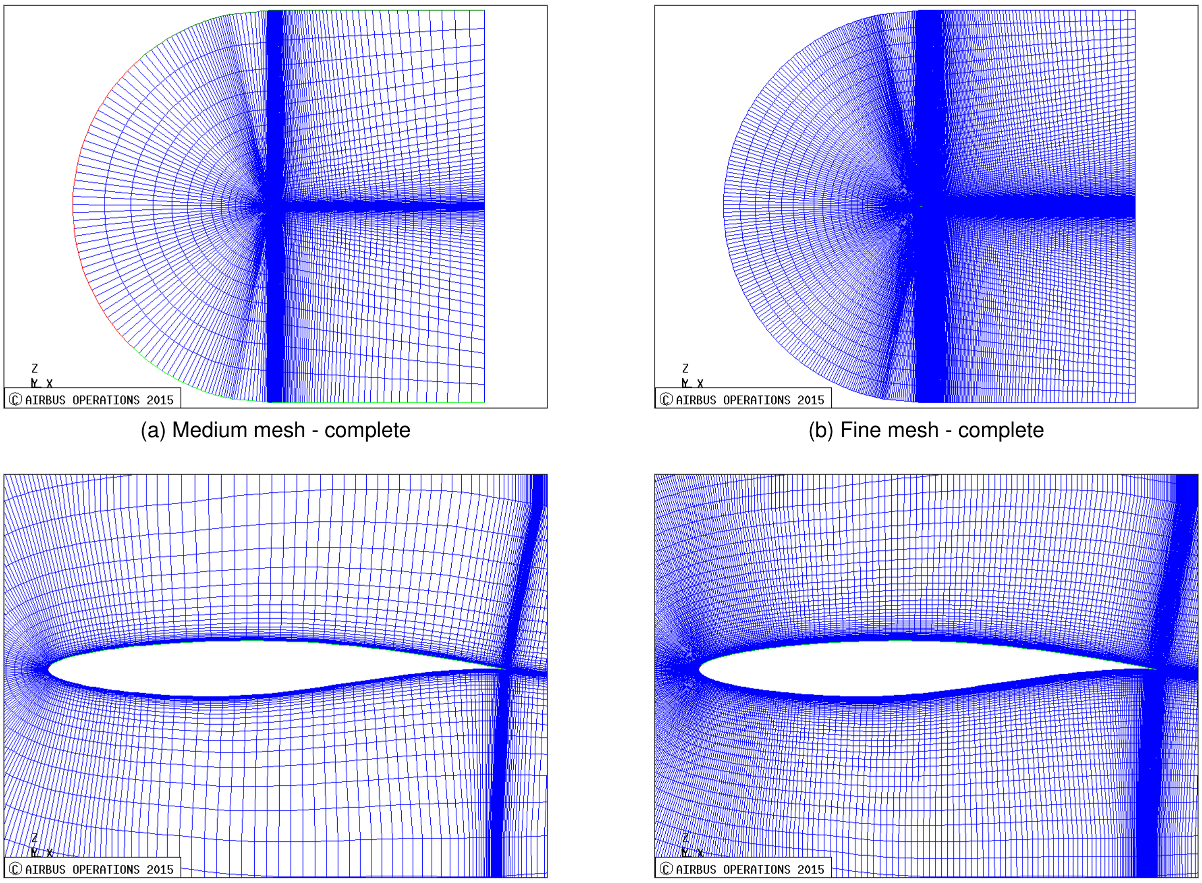

(a) Medium mesh - complete

(b) Fine mesh - complete

(c) Medium mesh - zoomed

(d) Fine mesh - zoomed

Figure 4.1: Mesh views

4.1.2 Baseline Design

Fig. 4.2 plots the ratio $\frac{C_{lp}}{C_d}$ versus C_{lp} for the above flight conditions. Hereinafter, an airfoil is said to be adapted if it is operating at a C_{lp} value $C_{lp} = C_{lp}^{\text{adaptation}}$ for which $\frac{C_{lp}}{C_d}$ is maximum. This point is of special interest because an aircraft usually cruises at maximum $\frac{C_{lp}}{C_d}$. It is therefore logical to increase the performances at this point. This means that the objective is to vertically translate the point:

$$\left(C_{lp}, \frac{C_{lp}}{C_d}\right)_{C_{lp}=C_{lp}^{\text{adaptation}}}$$

The maximum of $\frac{C_{lp}}{C_d}$ for the RAE2822 airfoil is at $C_{lp} = 0.63$, at which the values of Tbl. 4.2 are obtained. The residuals and history of both C_l and C_d of the corresponding flow solution are plotted in Fig. 4.3.

C_{lp}	C_l	AoA	C_d^{nf}	C_{df}	C_{dp}	C_d^{ff}	C_{dw}	C_{dv}	$-C_m$	$\frac{C_{lp}}{C_d^{nf}}$
0.63117	0.63119	1.848^{o}	103.2	59.61	43.55	100.0	4.56	95.47	0.0882	61.18

Table 4.2: Baseline RAE2822 - $C_{lp} = 0.630 \pm 0.001$

A first result extracted from Tbl. 4.2 is that the lift viscous component $C_{lv} \equiv C_l - C_{lp}$ is very small,

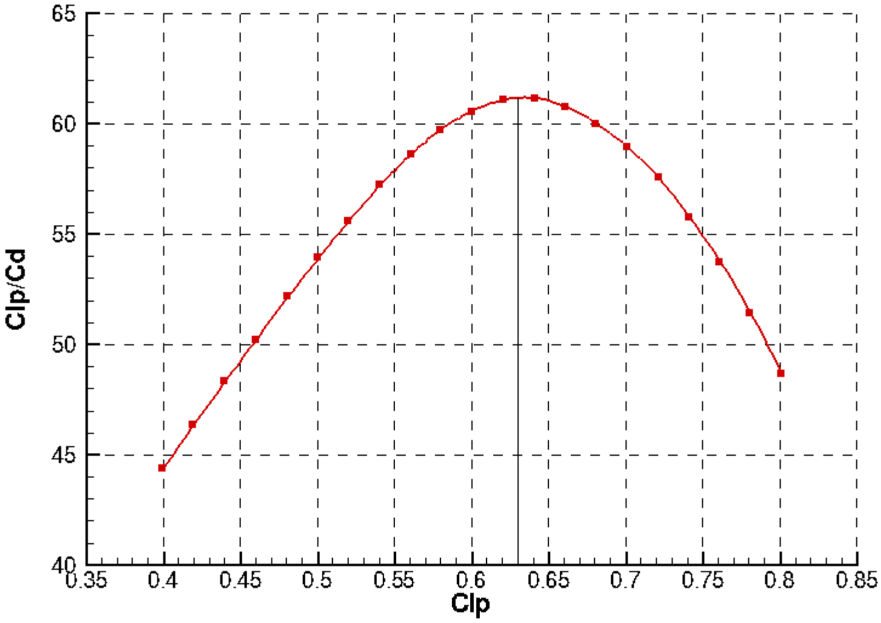

Figure 4.2: Baseline RAE2822 - $\frac{C_{lp}}{C_d}$ vs C_{lp} - Fine mesh

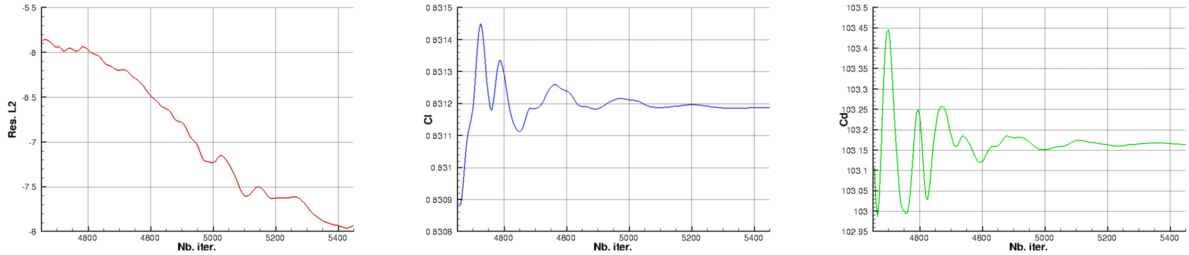

(a) L2 residuals

(b) C_l history

(c) C_d history

Figure 4.3: Convergence of flow solution for $C_{lp} = 0.630 \pm 0.001$ - Fine mesh

of the order 10^{-5}, justifying the integration of pressure alone for the lift coefficient as discussed in Section 2.1.5.4. At adaption, friction drag represents 57.8% of total drag, while pressure drag is responsible for the other 42.2%. A shock is present at around 55% of the chord, which can be seen in Fig. 4.4 resulting in 4.56 points of wave drag.

4.2 Problem Description

4.2.1 CT-Parameterization

The parameterization of the airfoil is decomposed in camber and half-thickness, that is, $y^{\pm}_{\text{airfoil}} = y_{\text{camber}} \pm y_{\text{half-thickness}}$. Both camber and half-thickness curves correspond to splines parameterized by three control points $\{0, 1, 2\}$. Each control point is defined by four values: x position, y position, tension T (stiffness of the spline) and angle α (angle of the spline with respect to the x axis). At certain points, one or more

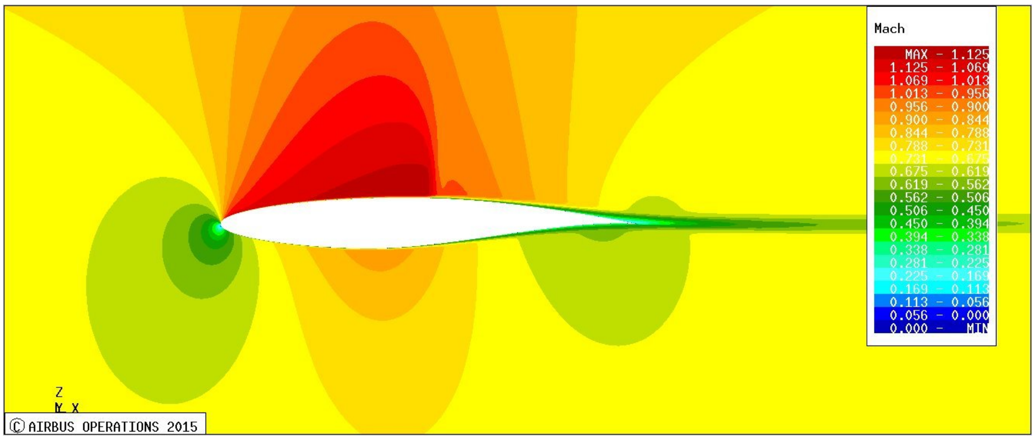

Figure 4.4: Baseline RAE2822 - Mach field - Fine mesh

of these values might be fixed (e.g. x position of point 0 is always 0). Tbl. 4.3 and Fig. 4.5 describe the parameterization of the airfoil.

	P0				**P1**				**P2**			
	x	y	α	T	x	y	α	T	x	y	α	T
Camber	0	0							1000	0		
Thickness	0	0	90^o				0^o		1000	0		

Table 4.3: Parameterization of RAE2822

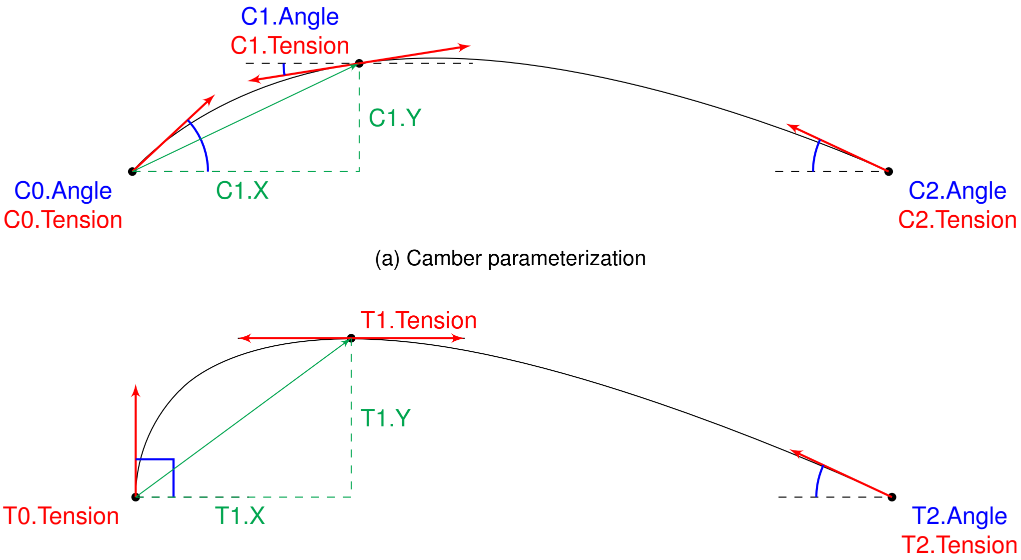

(a) Camber parameterization

(b) Thickness parameterization

Figure 4.5: Airfoil CT-Parameterization

`T0.Angle` and `T1.Angle` are both fixed because they represent the leading edge circle and maximum thickness point, respectively. From this reasoning, `T0.Tension` and `T1.Y` can be thought of as controlling the leading edge radius and the maximum half-thickness, respectively.

4.2.2 Design Space

Usually, when redesigning an airfoil, one is restricted to recambering because thickness is issued from structural/loading constraints. For this reason, the design space will match the parameterization of the camber line, that is: `C1.X`, `C1.Y`, `C0.Tension`, `C1.Tension`, `C2.Tension`, `C0.Angle`, `C1.Angle` and `C2.Angle`. The value range for each one is given in Tbl. 4.4.

Design Variable	**Lower Bound**	**Baseline**	**Upper Bound**	**Unit**
`C1.X`	100	394.8	900	mm
`C1.Y`	-20	1.915	$+20$	
`C0.Tension`	40	86.52	400	
`C1.Tension`		110.4		
`C2.Tension`		225.6		
`C0.Angle`	-15	-0.8047	$+15$	°
`C1.Angle`		1.546		
`C2.Angle`	-30	-7.653	0	

Table 4.4: Camber design value ranges

4.2.2.1 Normalization

One aspect of an optimization problem is the design space conditioning, which must be carefully studied. For example, in Tbl. 4.4, there are design variables whose value range is of the order 10^2 and others of the order 10^3. This is a possible issue from an optimizer point-of-view - since in Aerodynamics the design space is usually multimodal, that is, presents many local minima, the optimizer might fall into one local minima without exploring the design space.

Design space normalization comes as natural answer to this problematic behavior. There are two usual options for normalization: either normalize each variable value range to $[0, 1]$ or to $[-1, +1]$. The former is preferred to the latter when there is no ”starting design”, because the bounds are used as a reference. When the optimization is run from a ”baseline design”, the latter is preferred, since 0 is used as the reference for the baseline. This way, if the normalized design variable (e.g.: thickness) is negative, its non-normalized value has decreased, whereas a positive value corresponds to an increase.

Consider the design variable x, with lower bound l, upper bound u and baseline value b. The corresponding normalized variable is $\overline{x}$ and the basis of the design space normalization is the linear transformation (4.1).

$$x = T(\overline{x}) = \alpha\overline{x} + \beta \tag{4.1}$$

Ideally, all relations (4.2) would be valid. However, because the transformation is linear, unless the $[l, u]$ is centered around b (in this case $\frac{l+u}{2} = b$) only two of them can be respected at a time.

$$T(-1) = l \qquad T(0) = b \qquad T(+1) = u \tag{4.2}$$

As the primary objective of $[-1, +1]$ normalization is to have 0 as a baseline reference, $T(0) = b$ must always be respected. Furthermore, because we want to be able to generate all values in $[l, u]$, the other condition is chosen following Eq. (4.3).

$$\begin{cases} T(-1) = l & \text{if } b - l \geq u - b \\ T(+1) = u & \text{otherwise} \end{cases} \tag{4.3}$$

For example, consider the first case, where $T(-1) = l$ is to be respected. Coupled with $T(0) = b$:

$$\begin{cases} T(-1) = l \\ T(0) = b \end{cases} \Rightarrow \begin{cases} \alpha = b - l \\ \beta = b \end{cases} \Rightarrow T(\overline{x}) = (b-l)\overline{x} + b \Rightarrow \begin{cases} T(-1) = -(b-l) + b = l \\ T(0) = b \\ \boxed{T(+1) = (b-l) + b \geq (u-b) + b = u} \end{cases}$$

The last step shows that $u \in [T(-1), T(+1)] = [l, 2b - l]$. The value range for $\overline{x}$ is then restricted from $[-1, +1]$ to $[-1, T^{-1}(u)]$, where $T^{-1}(u) \leq +1$, such that the normalized design space corresponds exactly to the non-normalized one. Generally, the transformation is given by Eq. (4.4) and the normalized design space is given in Tbl. 4.5.

$$x = T(\overline{x}) = \max(b - l, u - b)\overline{x} + b \tag{4.4a}$$

$$\overline{x} \in \begin{cases} \left[-1, T^{-1}(u)\right] & \text{if } b - l \geq u - b \\ \left[T^{-1}(l), +1\right] & \text{otherwise} \end{cases} \tag{4.4b}$$

The effect of normalization is now calculated for a descending gradient method. Consider a descending gradient method on a normalized variable $\overline{x}$, then (γ is the step size):

$$\overline{x}_{n+1} = \overline{x}_n - \gamma \left.\frac{df}{d\overline{x}}\right|_{\overline{x} = \overline{x}_n}$$

Substituting by non-normalized variables:

$$\alpha^{-1}x_{n+1} + \alpha^{-1}\beta = \alpha^{-1}x_n + \alpha^{-1}\beta - \gamma\alpha \left.\frac{df}{dx}\right|_{x = x_n} \Rightarrow x_{n+1} = x_n - \gamma \left(\alpha^2 \left.\frac{df}{dx}\right|_{x = x_n}\right)$$

Frequently, in Aerodynamics, the design space is multimodal, that is, presents many local minima. This might be a risk, as the optimizer might fall into one local minima without exploring the design space. Fig. 4.6 illustrates this phenomenon and the normalization effect, where $\mathbf{D} = (x, y)^T$ and $\mathbf{D}_0 = (0, 0)^T$. Normalization is done to $[-1, +1]$ yielding $\alpha_x = 2$ and $\alpha_y = 1$. The true gradient on the non-normalized design space points in the direction of the local minimum. However, because the optimization and gradient are computed in the normalized design space, the x component of the gradient on the non-normalized design space is multiplied by $\alpha_x^2 = 4$ and the y component doesn't change because

$\alpha_y^2 = 1$. The step will then be taken in the direction of the modified gradient which doesn't point in the direction of the local minimum, possibly resulting in a better design space exploration. Obviously, this is a particular case - in fact the opposite case may happen, when the global minimum is switched with the local minimum and convergence speed takes a hit. However, as the main objective is not to fall *directly* into a local minimum without searching elsewhere, normalization is done.

Although SLSQP was chosen instead of a descending gradient algorithm, the first step of SLSQP is in fact equivalent to a descending gradient, since the Hessian matrix is the identity matrix at the beginning of the optimization.

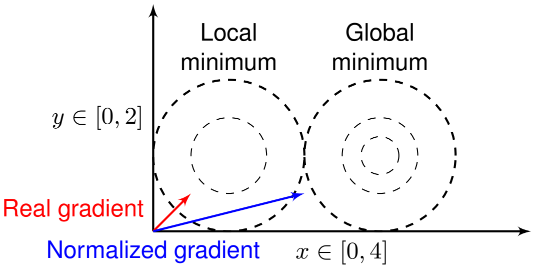

Figure 4.6: Normalization effect on gradient

Summarizing the many consequences:

- A descending gradient method on a normalized design space is not equivalent to the same descending gradient method on a non-normalized design space
- Each component of the gradient is multiplied by the corresponding variable scale factor α (not the same for all variables)
- It is more unlikely to fall in a local minimum without exploring the design space

This is a common technique in the domain of optimization, namely aerodynamic optimization and it will be used on both two and three-dimensional cases.

The resulting normalized space is given in Tbl. 4.5. It was however adapted, to always ensure a feasible geometry. Unfeasible geometries are the result of bad combinations of design variables values (e.g.: very low x and very high y values of C1) which are not feasible at VolDef level.

4.2.3 Optimization Problem

An optimization problem requires: an objective function, constraints (if there are any) and a design space. The design space was defined in Section 4.2.2, leaving the objective function and constraints to be defined. As discussed in Section 4.1.2, the baseline airfoil is adapted for $C_{lp} = 0.63$ and because aircraft usually flight at this point in cruise, it is logical to optimize at that condition. Furthermore, the adaptation $C_{lp} = C_{lp}^{\text{adaptation}}$ is to be kept constant at $C_{lp} = 0.63$.

The choice of objective function relies on one of the following C_{dp}, C_{df}, C_d. C_{dp} is chosen. Although it might seem inconsistent, since the objective is to minimize C_d, it is not. It is a way of stating that the objective is to minimize C_d by minimizing C_{dp}. Such a choice is due to the fact that the viscous adjoint

Design Variable	Lower Bound	Upper Bound	Adapted Lower Bound	Adapted Upper Bound
Norm.C1.X	-0.58349	$+1.0$	-0.2	$+0.65$
Norm.C1.Y	-1.0	$+0.82524$	-0.05	
Norm.C0.Tension	-0.14841	$+1.0$		
Norm.C1.Tension	-0.24320	$+1.0$		$+0.25$
Norm.C2.Tension	-1.0	$+0.93971$		
Norm.C0.Angle	-0.89817	$+1.0$		
Norm.C1.Angle	-1.0	$+0.81307$		
Norm.C2.Angle	-1.0	$+0.34244$		

Table 4.5: Normalized camber variables

terms in the current version of elsA-reverse are not very accurate, which is a known limitation. Furthermore, instead of computing two adjoint systems (C_{dp}, C_{df}), only one is computed, reducing computation time considerably.

Regarding the constraints, we will not impose any to begin with, since *a priori* there is no need to. The optimization problem is then defined in Eq. (4.5), for which the KKT conditions simplify to $\nabla C_{dp} = 0$ (if the considered design is not at the boundary of the design space), because the problem is unconstrained.

$$\underset{\mathbf{D}\equiv\text{camber,Target Lift}}{\text{minimize}} \quad C_{dp}|_{C_{lp}=0.63} \tag{4.5}$$

4.3 Unconstrained Optimization

Optimizations for solving Eq. (4.5) were run in the normalized design space.

4.3.1 Optimization Analysis

The history of both objective function and gradient norm (normalized by the baseline gradient) are shown in Fig. 4.7. The optimization takes 29 iterations to converge and 20 iterations to arrive to within 1% of the best value on the last iteration, for which the norm of the gradient is 5% of the baseline's. This is certainly close to the optimality condition $\nabla C_{dp} = 0$. The ”jumps” of the objective function occur at the same time as those of the gradient norm - the optimizer tries a certain search direction, which worsens the objective function that in turn appears on the gradient norm. Here, the gradient norm history serves the purpose of ”optimality monitor”.

The objective function starts at 47.36 and finishes at 41.12, translating into an objective function gain of 13.17%. These results are then validated on the fine mesh for a more precise aerodynamic analysis as discussed in Section 4.1.1.

The optimization took slightly more than 4 hours and 16 minutes running on 24 cores in a HPC cluster. The average computational time and average percentage of total computation time for each component of the toolchain are given in Tbl. 4.6.

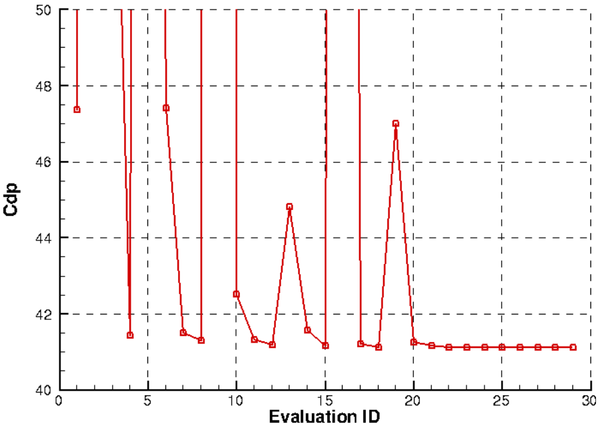

(a) Objective Function History

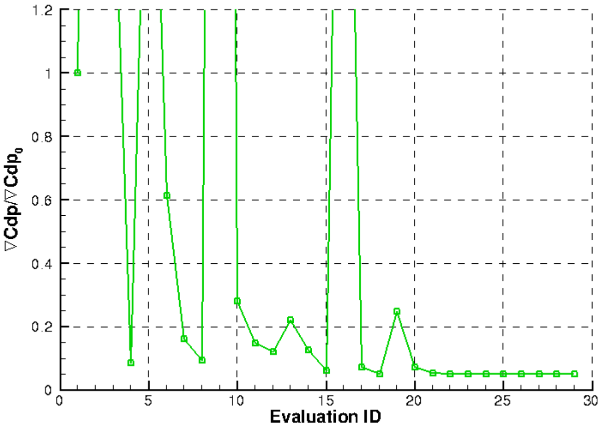

(b) Gradient Norm History

Figure 4.7: Unconstrained optimization history

	Padge	VolDef	elsA	ZAPP/ZAPP-rev	elsA-rev	VolDef-rev	Padge-rev
Time	12m23s	7m10s	2h12m06s	3m49s	1h31m56s	7m45s	1m29s
%	4.8	2.8	51.5	1.5	43.5	3.0	0.6

Table 4.6: Computation time

4.3.2 Aerodynamic and Geometry Analysis

A drag decomposition obtained with a far-field analysis of the optimized airfoil is given in Tbl. 4.7, the last row of which corresponds to the variation with respect to the baseline. The gain in C_{dp} is very close to the one calculated with the optimization values, validating the use of the ”medium” mesh. This gain globally results in a 4.95% gain in lift over drag ratio $\frac{C_{lp}}{C_d}$. Furthermore, wave drag is almost vanished on the optimized geometry. This is remarking, since wave drag is usually associated with thickness, which is kept frozen for this optimization. This reduction is easily seen in the C_p diagram Fig. 4.8a or in a Mach number field visualization Fig. 4.9. The shock strength is clearly reduced when comparing C_p with the baseline design on the upper side at around 50% of the chord.

	C_{lp}	α	C_d^{nf}	C_{df}	C_{dp}	C_d^{ff}	C_{dw}	C_{dv}	$-C_m$	$\frac{C_{lp}}{C_d^{nf}}$
Baseline	0.63117	$1.848°$	103.2	59.61	43.55	100.0	4.56	95.47	0.0882	61.18
Optimized	0.63011	$1.480°$	98.13	60.32	37.81	97.76	0.23	92.94	0.1075	64.21
Variation %	-0.17	-19.19	-4.91	1.19	-13.18	-2.24	-94.96	-2.65	21.88	4.95

Table 4.7: Optimized RAE2822 - Far-field drag decomposition - $C_{lp} = 0.630 \pm 0.001$

The increase of friction drag C_{df} is easily explained with the aid of Fig. 4.8b. The lower side curves are almost coincident. However, on the upper side at around 50%, the baseline curve drops well below the optimized one and remaining under the latter until the trailing edge. The drop is due to the already mentioned shock that occurs at that position - as the shock is stronger on the baseline design, after the shock, speed is lower than on the optimized design, which results in less local friction, which in turn results in less global friction drag.

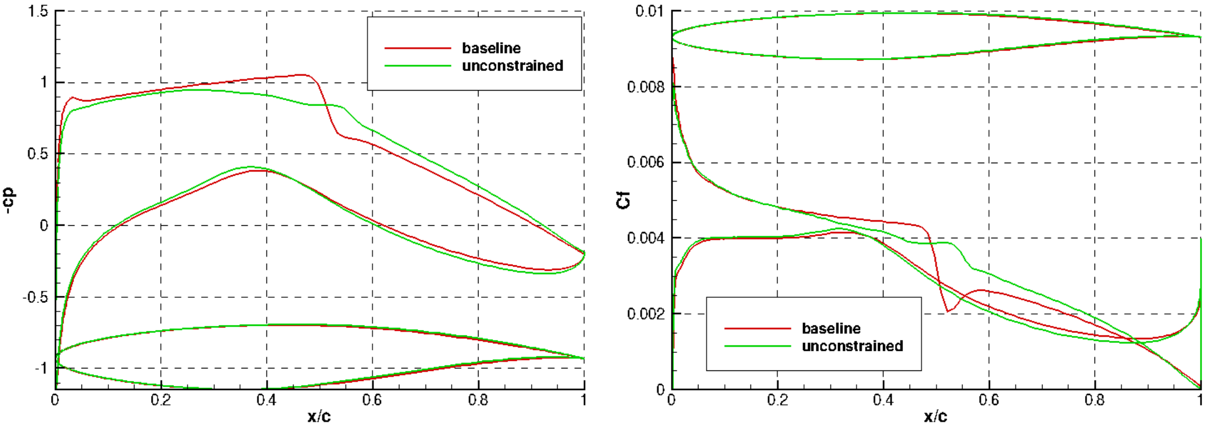

(a) C_p diagram

(b) C_f diagram

Figure 4.8: Unconstrained Optimized RAE2822 - C_p and C_f diagrams - Fine mesh

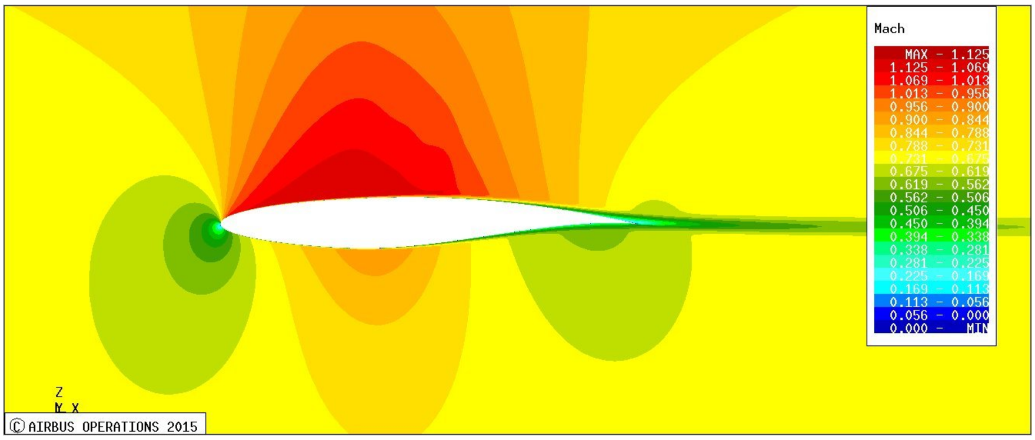

Figure 4.9: Optimized RAE2822 - Mach number field - Fine mesh

The airfoil geometry and camber line are shown in Fig. 4.10. The first 35% of the airfoil present a slightly positive camber, in contrast with the same region in the baseline, where camber starts slightly negative and becomes slightly positive. The biggest difference however, between the baseline and optimized airfoil, is found at around 76% of the chord where maximum camber occurs. It is increased by 24% with respect to the baseline, which explains the 18% increase in negative pitching moment, as the airfoil becomes more rear-loaded

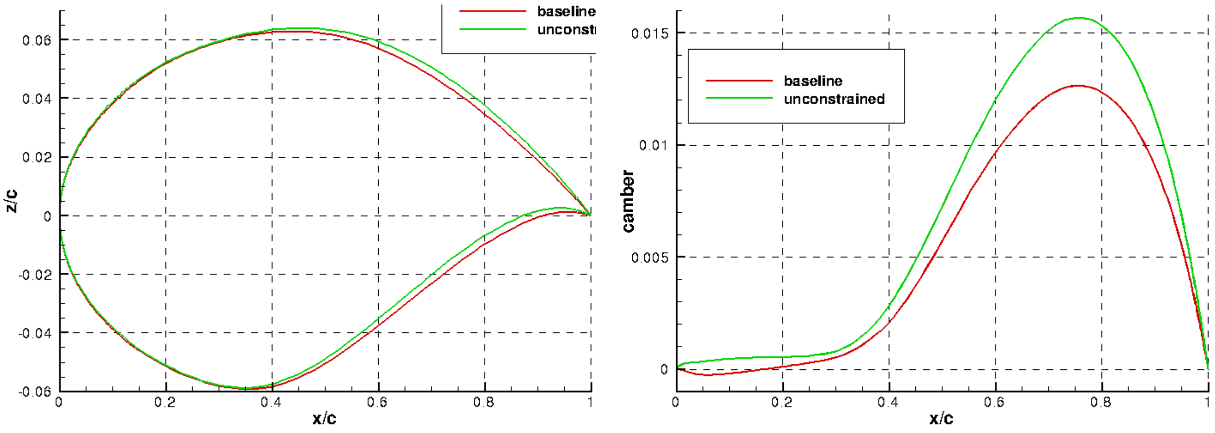

(a) Airfoil

(b) Camber

Figure 4.10: Unconstrained Optimized RAE2822 - Geometry

4.3.3 Global Behavior

The global lift-over-drag polar is shown in Fig. 4.11. It is clear that the optimized airfoil has a better performance than the baseline design. However, there is a shift of the adaptation C_{lp} of the airfoil to higher values. Consider an aircraft designed based on the baseline RAE2822 airfoil. Such an aircraft will fly at C_{lp} values around $C_{lp} = 0.63$. Thus, the big gain obtained for much higher C_{lp} will be unused. As this gain was probably obtained at the expense of performance in other flight conditions, the global result might not be positive at all. Furthermore, if we consider the usual wing-tail configuration aircraft, the much higher pitching moment will either require an increase of tail surface or an increase in elevator trim deflection, both increasing drag.

4.4 Constrained Optimization

4.4.1 Constrained Optimization Problem

Due to the adaptation shift phenomenon of the unconstrained optimization, a constraint must be imposed in order to keep the adaptation at $C_{lp} = 0.63$ (4.6).

$$\frac{d}{dC_{lp}} \left(\frac{C_{lp}}{C_d} \right)_{C_{lp}=0.63} = 0 \tag{4.6}$$

As this problem is solved numerically, the derivative (4.6) is approximated by finite differences

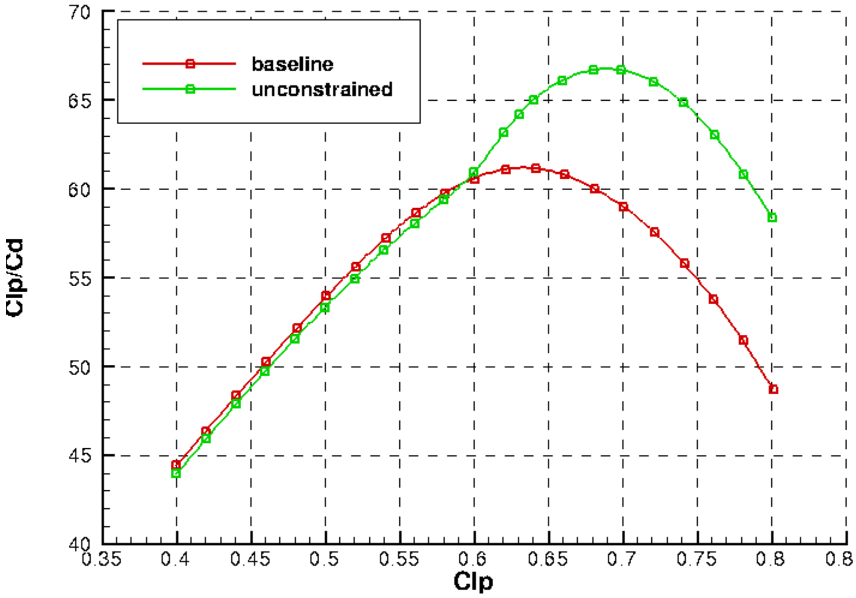

Figure 4.11: Baseline and Unconstrained Optimized RAE2822 - $\frac{C_{lp}}{C_d}$ polar - Fine mesh

$$\frac{d}{dC_{lp}}\left(\frac{C_{lp}}{C_d}\right)_{C_{lp}=0.63} = \frac{\left(\frac{C_{lp}}{C_d}\right)_{C_{lp}=0.63+\Delta C_{lp}} - \left(\frac{C_{lp}}{C_d}\right)_{C_{lp}=0.63-\Delta C_{lp}}}{2\Delta C_{lp}} + O\left(\Delta C_{lp}^2\right)$$

which gives the optimization problem in Eq. (4.7), where $(\cdot)_{\text{left}}$ and $(\cdot)_{\text{right}}$ correspond to $(\cdot)_{C_{lp}=0.63-\Delta C_{lp}}$ and $(\cdot)_{C_{lp}=0.63+\Delta C_{lp}}$, respectively. Hereinafter, ΔC_{lp} is written as Δ for a lighter nomenclature.

$$\begin{array}{ll} \underset{\mathbf{D},\text{Target Lift}}{\text{minimize}} & C_{dp}|_{C_{lp}=0.63} \\ \text{subject to} & \left(\frac{C_{lp}}{C_d}\right)_{\text{left}} = \left(\frac{C_{lp}}{C_d}\right)_{\text{right}} \end{array} \tag{4.7}$$

This constraint has some consequences at the computational performance level. Instead of requiring one flow solution per optimization iteration, it requires three ($C_{lp} = 0.63 - \Delta, 0.63, 0.63 + \Delta$). This does not majorly influence wall clock time, since all three computations are done in simultaneous. However, in order to run simultaneous computations, more computing resources are used. Furthermore, because the imposed constraint depends on C_{df}, there is an extra adjoint system to solve, resulting in extra computation time with respect to the unconstrained problem.

Finally, the optimality condition is then given in Eq. (4.8).

$$-\nabla C_{dp} = \lambda\left[\nabla\left(\frac{C_{lp}}{C_d}\right)_{\text{left}} - \nabla\left(\frac{C_{lp}}{C_d}\right)_{\text{right}}\right] \tag{4.8}$$

4.4.2 Influence of ΔC_{lp} and Optimization Analysis

Whenever using finite differences, one of the issues is the step value. To determine the best, four values are used and optimizations run for each: $\{0.005, 0.01, 0.03, 0.05\}$.

The history of both objective function and constraint is show in Fig. 4.12. The $\Delta = 0.05$ optimization finished very quickly in under thirty-five iterations - such a big step implies controlling points far apart, which might be difficult. For $\Delta = 0.03$, although it takes eighty iterations to end the optimization, the optimum value was already achieved at iteration thirty-six. The best optimization is that with $\Delta = 0.01$, beating the previous by almost one drag point. To confirm that this corresponds to the optimum step size, a final optimization with $\Delta = 0.005$ was run, finishing with an objective function final value even higher the $\Delta = 0.03$ optimization one.

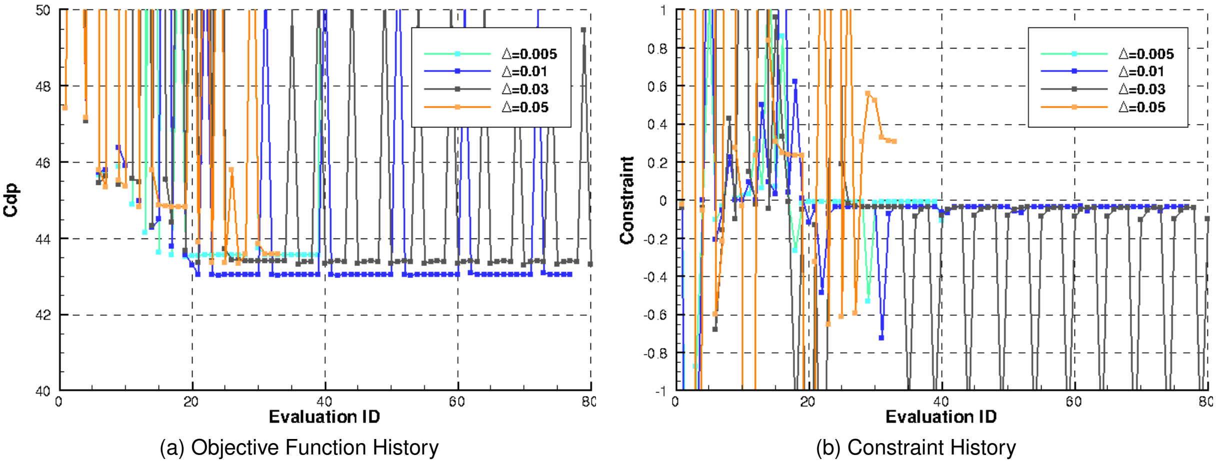

(a) Objective Function History

(b) Constraint History

Figure 4.12: Constrained optimization history

Hereinafter, the optimized airfoil obtained with $\Delta = 0.01$ will be called *constrained optimization airfoil*.

4.4.3 Aerodynamic and Geometry Analysis

The global lift-over-drag polar is shown in Fig. 4.13. As intended, the constrained optimization yields an airfoil whose adaptation is kept at the baseline's adaptation $C_{lp} = 0.63$. This results however in a small loss of 0.8 in $\frac{C_{lp}}{C_d}$ with respect to the unconstrained optimization. The gain in the region around $C_{lp} = 0.63$ is obtained in detriment of the outermost regions, where performance is lower than with the baseline.

A drag decomposition obtained with a far-field analysis of the optimized airfoil is given in Tbl. 4.8. The difference in performance between the unconstrained and constrained optimized airfoils is mainly in wave drag: whereas for the former $C_{dw} = 0.23$, for the latter $C_{dw} = 1.96$. This phenomenon is clearly seen in the C_p diagram Fig. 4.14a: the shock at around 45% of the chord is weaker than the baseline's, but much stronger than the unconstrained optimized airfoil's.

The increase in friction drag with respect to the baseline design, as well as the slight difference of the C_f diagram with respect to the unconstrained optimization follow the same reasoning as in Section 4.3.2. Finally, the pitching moment C_m in the constrained optimization is not as strong as in the unconstrained optimization.

The airfoil shape and its camber are shown in Fig. 4.15. Similarly to the unconstrained optimization, the constrained optimization produces an airfoil with higher aft-camber, although by a smaller amount. On both baseline and unconstrained optimized airfoils, camber is very small on the first 30% of the airfoil. On the contrary, the constrained optimized airfoil presents positive camber in this region.

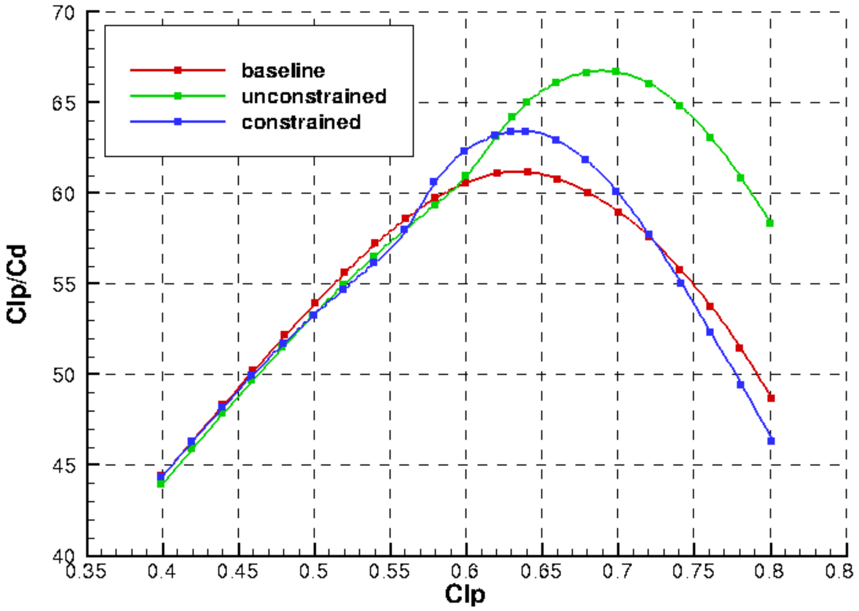

Figure 4.13: Baseline, unconstrained and constrained optimized RAE2822 - $\frac{C_{lp}}{C_d}$ polar - Fine mesh

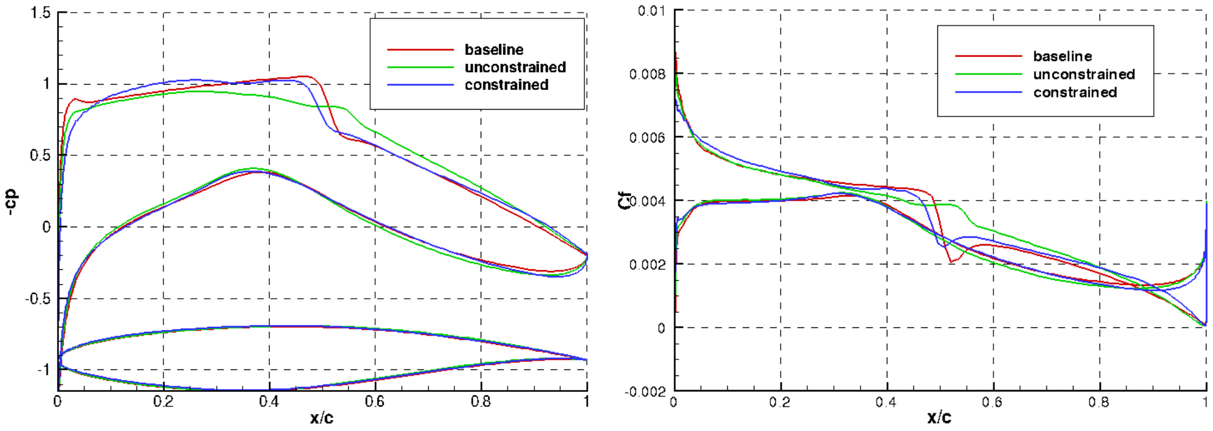

(a) C_p diagram

(b) C_f diagram

Figure 4.14: Constrained Optimized RAE2822 - C_p and C_f diagrams

	C_{lp}	α	C_d^{nf}	C_{df}	C_{dp}	C_d^{ff}	C_{dw}	C_{dv}	$-C_m$	$\frac{C_{lp}}{C_d^{nf}}$
Baseline	0.63117	1.848^{o}	103.2	59.61	43.55	100.0	4.56	95.47	0.0882	61.18
Unconstrained	0.63011	1.480^{o}	98.13	60.32	37.81	97.76	0.23	92.94	0.1075	64.21
Variation %	-0.17	-19.19	-4.91	1.19	-13.18	-2.24	-94.96	-2.65	21.88	4.95
Constrained	0.62980	1.449^{o}	99.37	60.04	39.33	99.09	1.96	92.71	0.0976	63.38
Variation %	-0.22	-21.59	-3.71	0.72	-9.69	-0.91	-57	-2.89	10.66	3.60

Table 4.8: Constrained Optimized RAE2822 - Far-field drag decomposition - $C_{lp} = 0.630 \pm 0.001$

As it was seen in Section 4.3.2, an increase of aft-camber produces:

- Adaptation C_{lp} shift
- C_{dw} reduction
- $-C_m$ increase

By not increasing aft-camber as much as on the unconstrained optimization, adaptation C_{lp} is shifted as much to the right. However, this implies that C_{dw} is not reduced as much as possible. On the other hand, positive for-camber counters both $-C_m$ increase and adaptation C_{lp} shift.

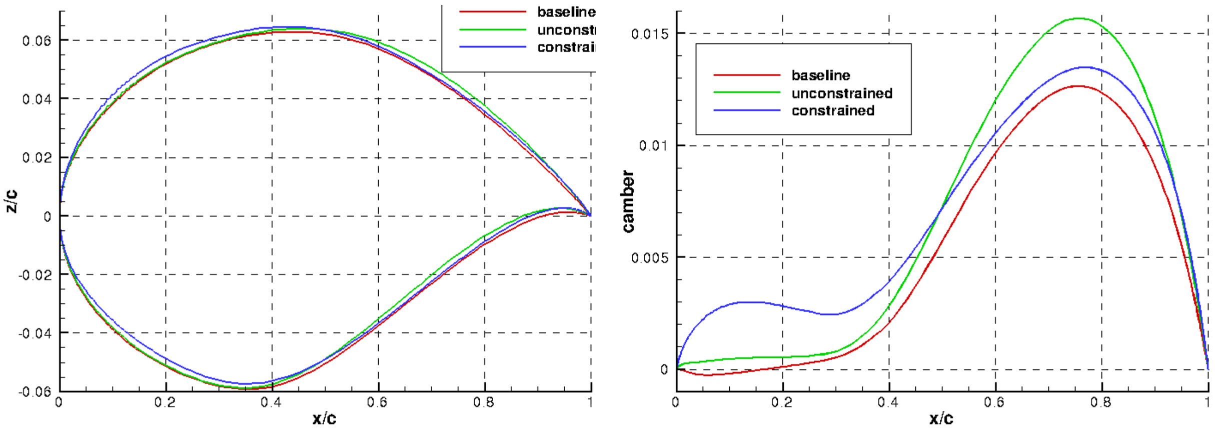

(a) Airfoil

(b) Camber

Figure 4.15: Constrained Optimized RAE2822 - Geometry

4.5 Changing Adaptation C_{lp}

4.5.1 Optimization Problem

Following the last section, it is logical to wonder if the adaptation of the airfoil can willingly be changed to a desired value of C_{lp}. Furthermore, what's the global behavior (i.e.: polar) and characteristics of the airfoil.

As such, a modification to (4.7) must be made: the constraint is applied at $C_{lp} = C_{lp}^*$ instead of $C_{lp} = 0.63$. Moreover, $\Delta = 0.01$ is used, as discussed in Section 4.4.2. Finally, the resulting problem is given in Eq. (4.9).

$$\begin{array}{ll} \underset{\mathbf{D},\text{Target Lift}}{\text{minimize}} & C_{dp}|_{C_{lp}=C_{lp}^*} \\ \text{subject to} & \left(\frac{C_{lp}}{C_{dp}}\right)_{C_{lp}=C_{lp}^*-0.01} = \left(\frac{C_{lp}}{C_{dp}}\right)_{C_{lp}=C_{lp}^*+0.01} \end{array} \tag{4.9}$$

Since the unconstrained optimization shifts the adaptation to higher C_{lp} values, C_{lp}^* is chosen smaller than $C_{lp} = 0.63$. Two values were chosen: $C_{lp}^* = 0.60$ close to the baseline adaptation and another $C_{lp}^* = 0.54$ far from the baseline adaptation.

4.5.2 Optimization Analysis

The history of the objective function and constraint are shown in Fig. 4.16. The best gain of the objective function is obtained for $C_{lp}^* = 0.63$, which was discussed in Section 4.4. The $C_{lp}^* = 0.60$ results in a small reduction of C_{dp} of 1.98%, corresponding to iteration 79. This gain is small due to the very high initial constraint value. For $C_{lp}^* = 0.54$, the objective function is worsened in order to satisfy the constraint, which starts with the biggest value of all optimizations, resulting in a 7.95% increase of C_{dp}.

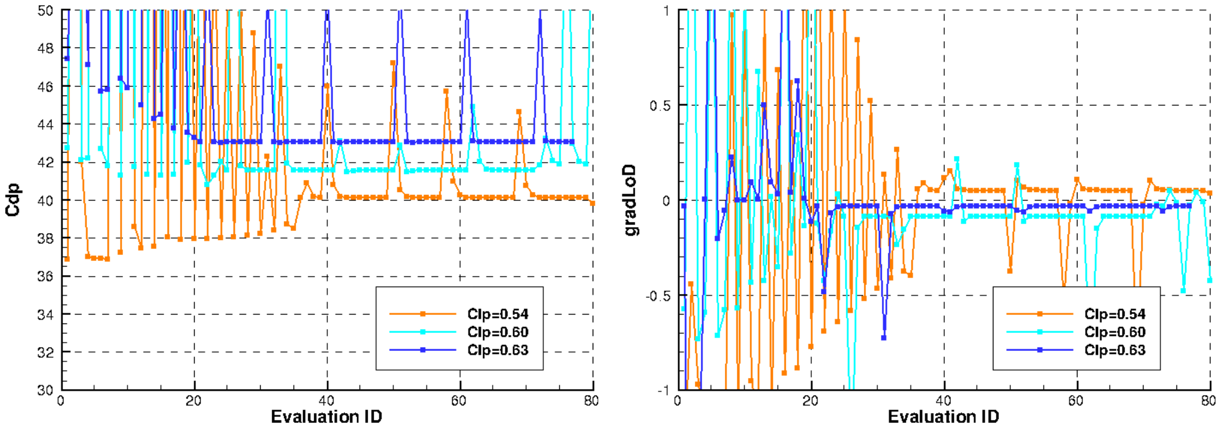

(a) Objective Function

(b) Constraint

Figure 4.16: Changing adaptation - Optimization history

4.5.3 Aerodynamic and Geometry Analysis

The global lift-over-drag polar is shown in Fig. 4.17. It is clear that each polar is centered around the intended value of C_{lp}. Commentaries on the $C_{lp}^* = 0.63$ have been made in previous sections. The $C_{lp}^* = 0.60$ slightly improves performance in $C_{lp} \in [0.55, 0.61]$ in detriment of a slight loss of performance below $C_{lp} = 0.55$ and a major loss of performance above $C_{lp} = 0.61$. In the case of $C_{lp}^* = 0.54$, there is a global loss of C_{lp}/C_d.

The far-field drag decomposition analysis for all three optimized airfoils and the corresponding baseline values are given in Tbl. 4.9. Regarding $C_{lp}^* = 0.54$, there is an increase in C_d of 1.5%, resulting

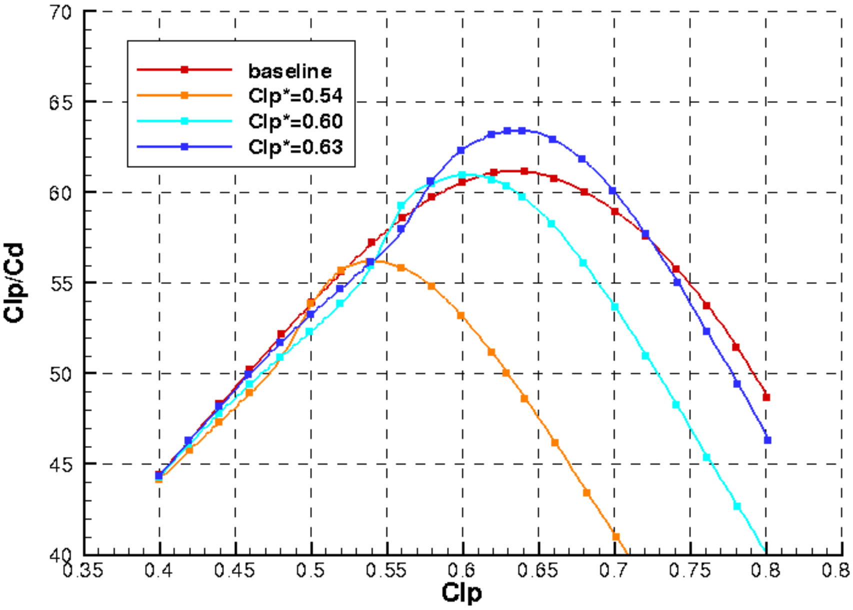

Figure 4.17: Optimized designs - $\frac{C_{lp}}{C_d}$ polar

in a loss of -1.83% in C_{lp}/C_d, mostly due to the huge increase in wave drag. The $C_{lp}^* = 0.60$ has a particular feature: C_{dw} does not change. The slight 0.68% improvement in C_{lp}/C_d is due to a reduction of viscous pressure drag $C_{dvp} = C_{dv} - C_{df}$, which is 33.96 for the baseline design and 31.74 for the optimized design. Both affirmations can be confirmed with the aid of the C_p diagrams in Fig. 4.18. The C_p distribution for $C_{lp}^* = 0.60$ shows a more intense suction on the upper side before 45% of the chord and a less intense suction on both upper and lower sides after that point, resulting in an overall reduction of viscous pressure drag.

	C_{lp}	C_d^{nf}	C_{df}	C_{dp}	C_d^{ff}	C_{dw}	C_{dv}	C_{dsp}	$-C_m$	$\frac{C_{lp}}{C_d^{nf}}$
Baseline	0.54060	94.44	60.53	33.92	92.14	0.44	91.70	2.30	0.0885	57.24
Optimized	0.53868	95.86	59.84	36.02	95.56	1.89	90.35	0.31	0.0629	56.19
Variation %	-0.36	1.50	-1.14	6.19	3.71	329.55	-1.47	-86.52	-28.93	-1.83
Baseline	0.60015	99.08	59.99	39.10	96.26	2.31	93.95	2.82	0.0882	60.57
Optimized	0.59969	98.34	60.05	38.29	98.14	2.31	91.79	0.20	0.0912	60.98
Variation %	-0.08	-0.75	0.10	-2.07	1.95	0.00	-2.30	-92.91	3.39	0.68
Baseline	0.63117	103.2	59.61	43.55	100.0	4.56	95.47	3.12	0.0882	61.18
Optimized	0.62980	99.37	60.04	39.33	99.09	1.96	92.71	0.28	0.0976	63.38
Variation %	-0.22	-3.71	0.72	-9.69	-0.91	-57	-2.89	-91	10.66	3.60

Table 4.9: Optimized RAE2822 at $C_{lp} = \{0.54, 0.60, 0.63\} \pm 0.001$

Both airfoil and camber shapes for the optimized designs are show in Fig. 4.19. Both designs present the same behavior with respect to the baseline: increase forward camber and reduce aft-camber. This was expected, since the optimization for $C_{lp}^* = 0.63$ in Section 4.4 already showed the same tendencies.

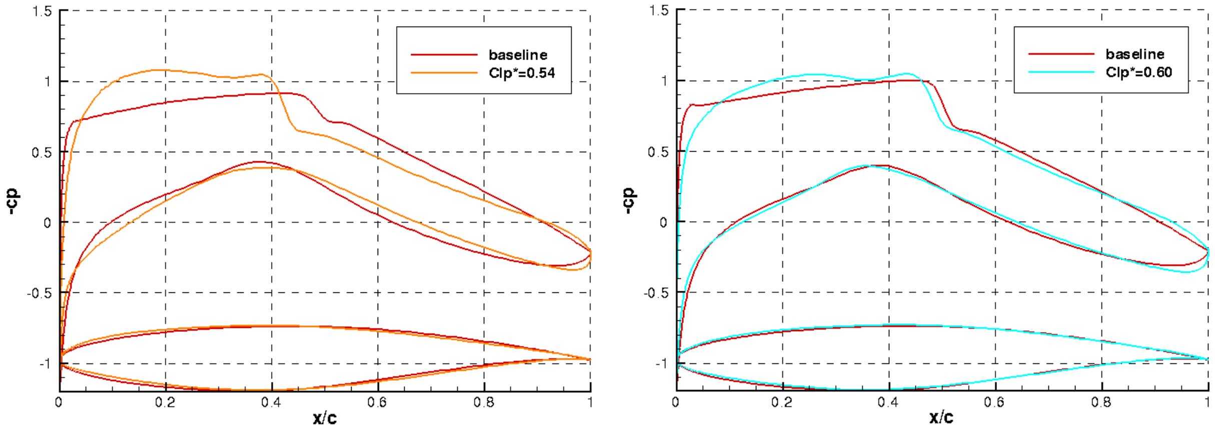

(a) Optimized for $C_{lp} = 0.54$

(b) Optimized for $C_{lp} = 0.60$

Figure 4.18: Changing Adaptation Optimized RAE2822 - C_p diagram

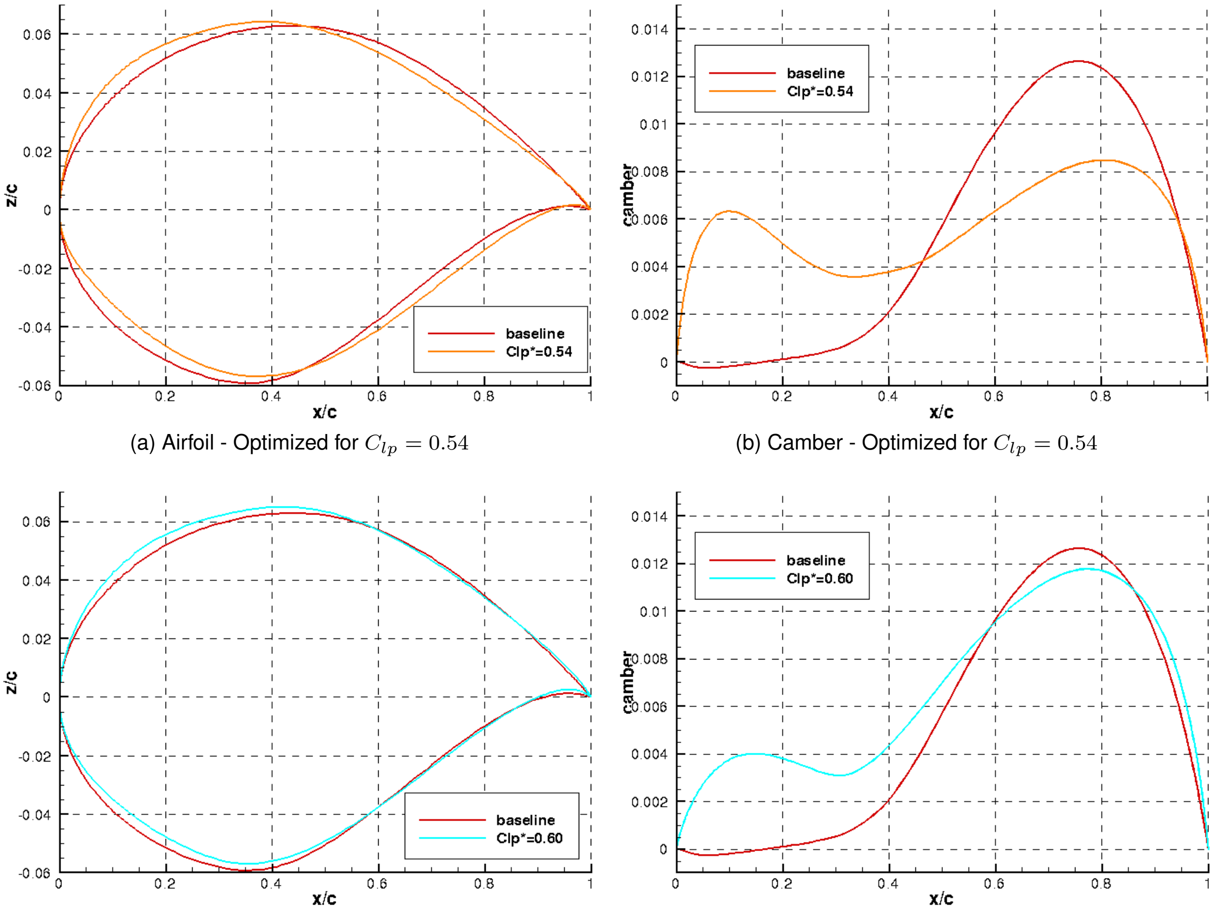

(a) Airfoil - Optimized for $C_{lp} = 0.54$

(b) Camber - Optimized for $C_{lp} = 0.54$

(c) Airfoil - Optimized for $C_{lp} = 0.60$

(d) Camber - Optimized for $C_{lp} = 0.60$

Figure 4.19: Changing Adaptation Optimized RAE2822 - Geometry

4.6 Conclusion

The objective of the original optimization problem was set as improving the value of maximum $\frac{C_{lp}}{C_d}$, which occurs at $C_{lp} = 0.63$, by minimizing C_{dp} at the same point. This was the result of a reasoning based on the fact that aircraft usually cruise at that point. The choice of C_{dp} over C_d is based on a known limitation of the current version of elsA-reverse that is not very accurate on the viscous terms.

Without any further information, an unconstrained optimization was attempted. This optimization yielded good results in terms of reducing C_{dp} (and indirectly C_d) at $C_{lp} = 0.63$. However, plotting the $\frac{C_{lp}}{C_d}$ polar of the new optimized design showed that the maximum of $\frac{C_{lp}}{C_d}$ no longer is at $C_{lp} = 0.63$, having been shifted to higher values. This behavior is undesired, demonstrating that a reformulation of the problem was needed. Such a reformulation came in the form of an equality constraint, stating that the derivative of $\frac{C_{lp}}{C_d}$ with respect to C_{lp} was to vanish at $C_{lp} = 0.63$.

The new problem required an extra adjoint system to be solved, because of the addition of C_{df} in the form of C_d in the constraint and two more computations per optimization iteration. Both effects result in an increase in wall clock and CPU computation time. The new optimized design was slightly less performing than the unconstrained one at $C_{lp} = 0.63$. It respected nevertheless the constraint, keeping the maximum of $\frac{C_{lp}}{C_d}$ at $C_{lp} = 0.63$.

A natural question followed: is it possible to willingly change the location of the maximum of $\frac{C_{lp}}{C_d}$ to a desired value of $C_{lp} = C_{lp}^*$. It was shown it is indeed possible, but at the expense of $\frac{C_{lp}}{C_d}$.

Globally, the optimization chain was shown to be sufficiently robust to improve an airfoil that already has a good performance. Moreover, this improvement was done with a limited selection of design variables and under imposed constraints.

Chapter 5

Winglet Optimization

This section deals with a long range wide-body twin-engine jet airliner designed by Airbus. The objective is to reshape its winglet by retwist, recamber and planform redefinition.

5.1 Test Case Definition

The flight conditions are given in Tbl. 5.1.

Parameter	**Value**
Re	5.652×10^6
M	0.82
C_{Lp}	0.55

Table 5.1: Flight Conditions

5.1.1 Mesh

The mesh was generated in ANSYS ICEM and was coarsed to medium and coarse meshes. They are composed of 1734 blocks and comprise 18187074 and 4195548 nodes, respectively. It does not include an Horizontal Tail Plane. Optimizations will be run on the coarse mesh, in order to save on computation time. The body surface mesh in the coarse mesh is shown in Fig. 5.1.

5.1.2 Parameterization

The winglet is defined by eight sections, called AF`x`, where `x` is the number of the section, as can be seen in Fig. 5.2a. The first three sections are not changed, in order to assure a smooth continuity between the wing and the winglet. The airfoils of each of the last five sections is controlled by three control points, as can be seen in Fig. 5.2b, to which a twist angle is applied.

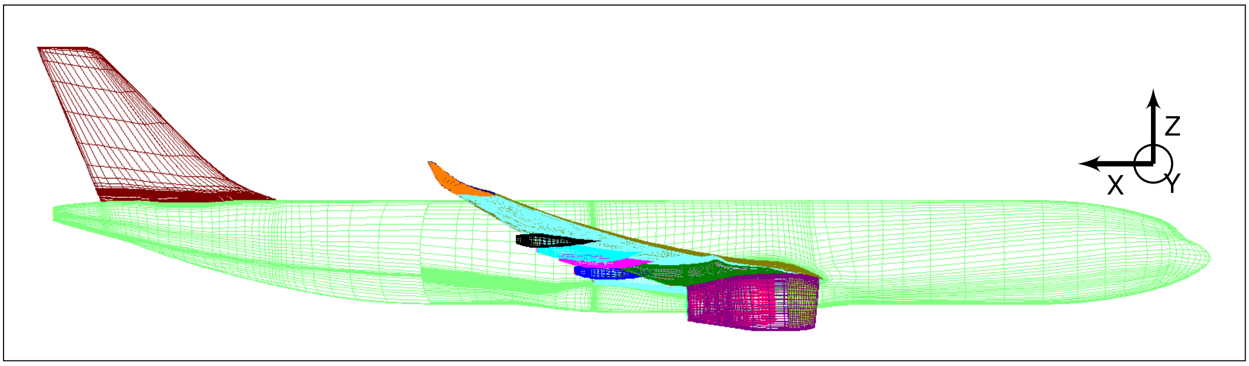

Figure 5.1: Body surface mesh - Coarse mesh

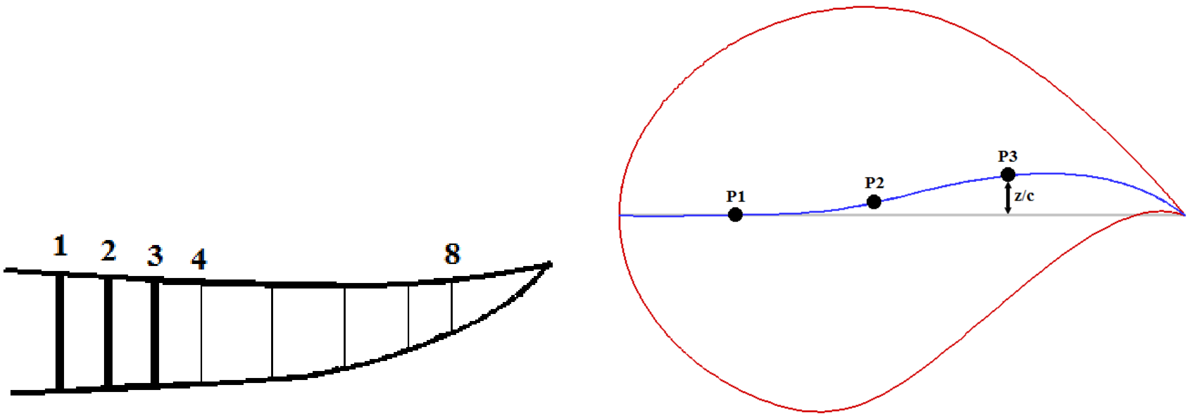

(a) Winglet shape with parameterized sections

(b) Winglet section airfoil parameterization

Figure 5.2: Winglet parameterization

Summarizing, the planform is parameterized by four parameters: span, height, sweep angle and taper ratio; and by five sections, each having four design variables: section twist angle and z coordinate of three control points of the camber line. This results in a design space of dimension 24.

The bounds of the modification to the baseline for each design variable is given in Tbl. 5.2. All design variables are normalized between $[-1;+1]$, where 0 corresponds to the baseline design. The sweep angle is however limited to $[-1;+0.5]$.

Variable	**Bounds**
Twist	$\pm 2^o$
Zcp	$\pm 3\%$
Span	± 0.5 m
Height	± 0.5 m
Sweep Angle	$\pm 10^o$
Taper	± 0.015

Table 5.2: Bounds of modification to baseline design

5.1.3 Optimization Problem

The objective function of this optimization problem is the pressure drag C_{Dp}. Furthermore, a maximum load constraint on the winglet is imposed. The problem is mathematically stated in Eq. (5.1).

$$\begin{aligned} \underset{\mathbf{D},\text{Target Lift}}{\text{minimize}} \quad & C_{Dp}|_{C_{Lp}=0.55} \\ \text{subject to} \quad & (C_{Lp})_{\text{winglet}} \leq (C_{Lp})_{\text{winglet}}^{\text{max}} \end{aligned} \tag{5.1}$$

The KKT conditions for this problem are given in Eq. (5.2). Eq. (5.2b) separates in two conditions: $\mu = 0$ or $(C_{Lp})_{\text{winglet}} = (C_{Lp})_{\text{winglet}}^{\text{max}}$. In the first case, Eq. (5.2a) becomes $\nabla C_{Dp} = 0$, the optimality condition in unconstrained problems. In the second case, the gradient of C_{Dp} must be on the opposite direction of the gradient of $(C_{Lp})_{\text{winglet}}$ at the boundary of the domain. Eq. (5.2a) is usually evaluated by the KKT angle, that is, the angle between both gradients $\theta\left[\nabla C_{Dp}, \nabla\left(C_{Lp}\right)_{\text{winglet}}\right]$.

$$-\nabla C_{Dp} = \mu \nabla \left(C_{Lp}\right)_{\text{winglet}} \tag{5.2a}$$

$$\mu\left[(C_{Lp})_{\text{winglet}} - (C_{Lp})_{\text{winglet}}^{\text{max}}\right] = 0 \tag{5.2b}$$

5.2 Design of Experiments

With such complex geometry and aerodynamics, aggravated by the high number of design space dimensions, it is difficult to grasp a sense of the design space. Exploring the design space seems the necessary step to begin such a complex study. The DOE comes as a natural design space exploration method. It is a powerful tool and can be used with multiple objectives:

- Exploration of the design space
- Identification of unfeasible designs (bad combination of design variables values)
- Identifying the relation between the objective function and the constraint
- Design variable influence analysis
- Rough sense of the best design
- Seed - take a good design (arbitrary criteria) with which to start an adjoint optimization

Yet, it presents some drawbacks:

- Because the DOE doesn't take constraints into account, if the objective is to optimize with constraints, many of the generated solutions might not respect the constraints
- As the number of dimensions of the design space grows larger, the required number of points to have a significant sample grows exponentially

The second drawback is particularly important, since in industrial aerodynamics, such as this case, the number of design variables ranges from tens to hundreds.

Furthermore, each DOE sample follows the following steps, all of which are not computationally trivial:

1. Generate samples
2. CAD generation - Surface
3. Mesh deformation
4. CFD
5. Post-processing

For the current case, a DOE on all 24 design variables was run with the Latin Hypercube Sampling Algorithm. A total of 500 samples were generated, taking a total wall clock time of 10 days, each sample running on 48 cores on an HPC cluster.

5.2.1 Identification of problematic combinations of design variables values

Certain combinations values of design variables are said to be problematic if they make VolDef fail. This happens when the resulting shape is highly deformed, rendering impossible the task of volume deformation. For example, if the position of the first control point of the airfoil is too close to the leading edge in x and far away in y, the airfoil will have a ”zig-zag” shape.

When optimizing (adjoint or not), the risk of VolDef failing should be minimized. In order to do this, a visual correlation analysis between design variables and VolDef failing was done. It was found that, as can be seen in Fig. 5.3, under a certain critical value of `Sweep Angle` close to 0, the density of failed designs is higher than above that same value.

However, since this density is still acceptable, the range of this design variable won't be modified.

5.2.2 Relation between the objective function and constraint

A scatter plot of the objective function with respect to the constraint is shown in Fig. 5.4. It clearly shows that they are anti-correlated, meaning that the constraint can not be removed. Furthermore, it shows that the case $\mu = 0 \Rightarrow \nabla C_{Dp} = 0$ of Eq. (5.2) is highly unlikely, or conversely, that the optimum is very likely to be on the boundary of the valid domain $(C_{Lp})_{\text{winglet}} = (C_{Lp})_{\text{winglet}}^{\text{max}}$.

5.2.3 Design variable influence analysis

The selection of design variables is one of the most important aspects in an optimization problem. If this selection isn't well suited, the optimization will not achieve good results. For example, an optimization where the objective is to have an auto-stable airfoil - such a design must have a positive trailing edge angle - with a design space which only allows negative trailing edge angles won't yield very good results.

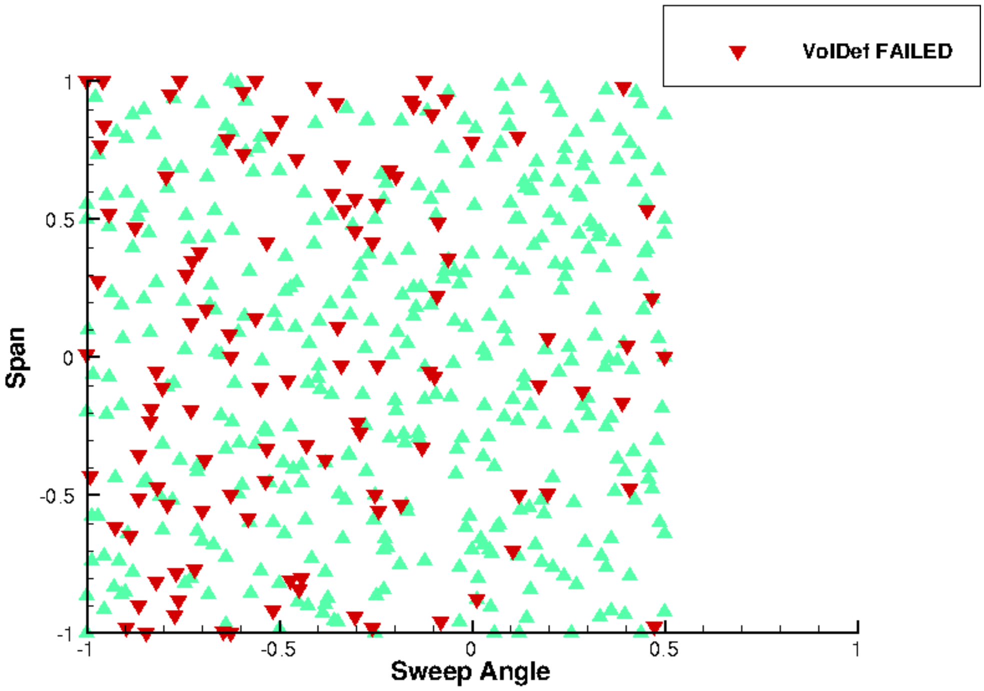

Figure 5.3: Failed designs in `Span` vs `Sweep Angle`

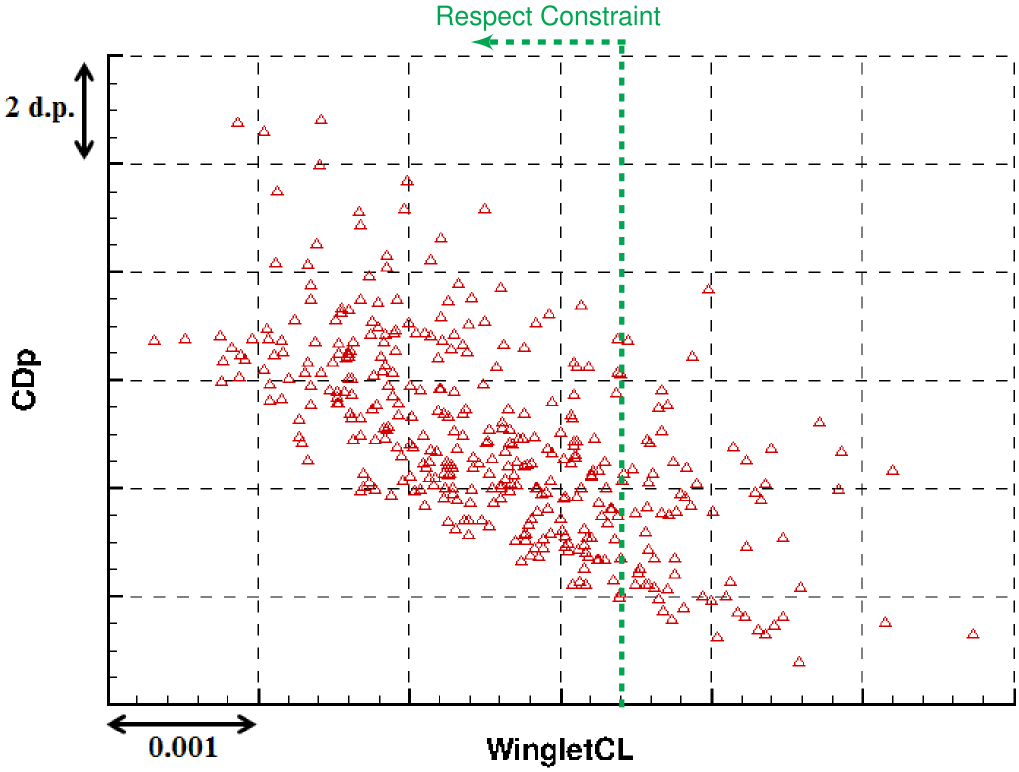

Figure 5.4: C_{Dp} vs $(C_{Lp})_{\text{winglet}}$

Furthermore, there may be some design variables whose influence is almost nonexistent. Identifying and possibly eliminating these variables can be important for reducing the design space, possibly increasing the convergence speed.

From the 500 samples, 377 were successfully analyzed with CFD and post-processed with a far-field analysis. This yields the following outputs: $C_{Dp} \equiv \texttt{DragP}$, $(C_{Lp})_{\text{winglet}} \equiv \texttt{WingletCL}$, $\alpha \equiv \texttt{AoA}$, $C_D^{nf} \equiv \texttt{CD NF}$, $C_D^{ff} \equiv \texttt{CD FF}$, C_{Dw}, C_{Di}, C_{Dvp}, C_{Df}, C_{Dsp} and $C_M \equiv \texttt{CPitch}$; on which the influence analysis is done, using the Sensitivity and Dependency Analysis tool of MACROS [24]. This tool is composed of three sequential components:

- Checker: checks if there is a dependency between an input X and output Y (for all pairs (X, Y)) and if it is statistically significant

- Ranker: ranks all inputs according to each input's importance

- Selector: selects the most suitable input subset to construct an approximate model

5.2.3.1 Checker

The checker computes a *correlation score* and a *p-value*. The *correlation score* is a number in $[-1; +1]$, where 0 means that Y does not depend on X and ± 1 means that Y is a deterministic function of X ($+1$ if Y increases with X and -1 otherwise). *p-value* is the probability that a correlation was found on the given sample while Y does not depend on X in reality. In other words, it's the probability that the true correlation score is (near) 0 and that the observed correlation score $\neq 0$ appeared by chance. The common threshold for *p-value* is 5%, which is considered small enough to be sure that the correlation is significant.

Two analysis were made, with two different correlation score functions: Pearson's correlation score, which can find linear dependencies; distance correlation score, which is a state-of-the-art metric and can find any type of dependence. Fig. 5.5 shows the results of the checker analysis. There are nine inputs marked with black rectangles, corresponding to inputs which are not correlated with any of the outputs Tbl. 5.3. Furthermore, both linear and general correlation functions give exactly the same results, which might indicate that for the current design space, the dependencies might be linear. The inputs in Tbl. 5.3 are eliminated and are not fed to the Ranker.

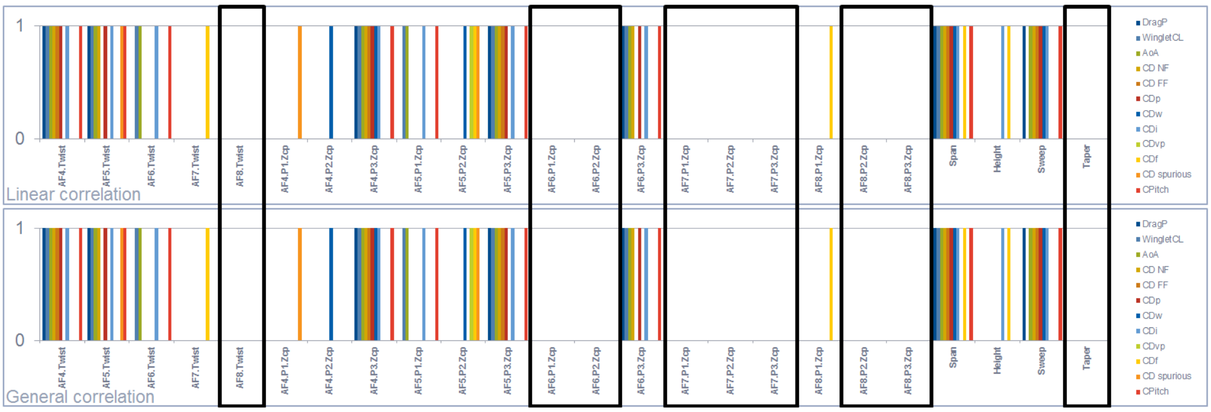

Figure 5.5: SDA Checker - Results

Taper	AF8.Twist	AF7.P1.Zcp
AF6.P1.Zcp	AF8.P2.Zcp	AF7.P2.Zcp
AF6.P2.Zcp	AF8.P3.Zcp	AF7.P3.Zcp

Table 5.3: Inputs not correlated with any of the outputs

5.2.3.2 Ranker

The ranker computes the ”importance” of each input according to some criteria (a measure of the effect of input X on output Y), with the objective of ranking them. This ranking gives a rough idea of how much an input is more or less important with respect to the others.

Two types of score are available: Screening indices - crude estimation of the average partial derivative of each input; Sobol indices - estimation of the variance of the output due to the variance of the input. A ranking analysis must be done for each output. At this point however, focus is given to C_{Dp} and $(C_{Lp})_{\text{winglet}}$, since these are the most relevant outputs for the problem at hand. Moreover, only one ranking type is used, such as to not grow the ”tree” of cases. The results of the Ranker are shown in Fig. 5.6, from which the ranking in Tbl. 5.4 will be fed to the Selector.

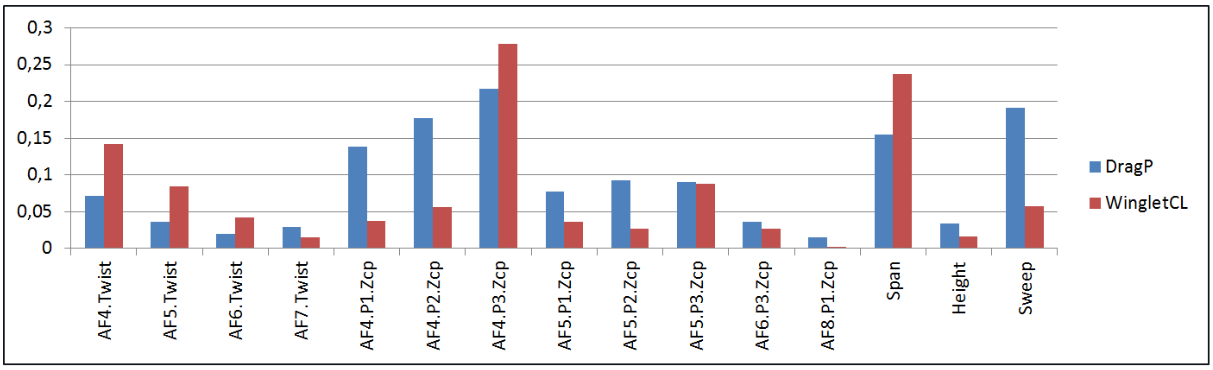

Figure 5.6: SDA Ranker - Results

1	2	3	4	5
AF4.P3.Zcp	Span	Sweep Angle	AF4.P2.Zcp	AF4.P1.Zcp
6	7	8	9	10
AF5.P3.Zcp	AF5.P2.Zcp	AF5.P1.Zcp	AF4.Twist	AF5.Twist
11	12	13	14	15
A6.Twist	AF6.P3.Zcp	Height	AF7.Twist	AF8.P1.Zcp

Table 5.4: SDA Ranker - Input Ranking

Note that Height is in the 13th position. This might seem counter-intuitive, since height is an important parameter of a winglet. This paradox is easily solved by analyzing a plot of C_{Dp} vs Height *for a restricted range of span*, as in Fig. 5.7. There is a clear anti-correlation between C_{Dp} and Height, which is not seen if designs with varying Span are plotted.

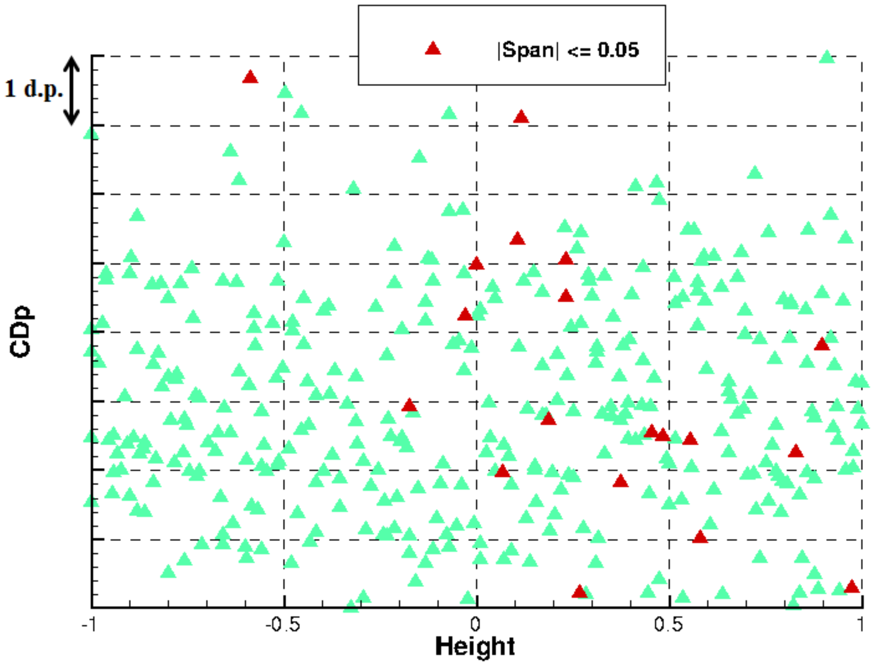

Figure 5.7: C_{Dp} vs $\texttt{Height}$ for $|\texttt{Span}| \leq 0.05$

The dependencies of C_{Dp} on the first four variables of the ranking Tbl. 5.4 are shown in Fig. 5.8.

5.2.3.3 Selector

The objective of the Selector is to select the smallest subset of inputs that provides the best possible approximation quality. The algorithm iteratively modifies the subset based on the ranking computed in the previous step. For every subset, an approximated model is constructed and its quality assessed. The subset with the minimum approximation error and of the smallest size is chosen. The approximation error can be accounted with respect to: all outputs, a subset of outputs or one output. There are two types of subset search: full search - tests all 2^{15} possible subsets, which is impractical; AddDel - runs sequential series of adds/deletes of inputs to/from the subset.

Two analysis were made, both with the AddDel method: all outputs are taken into account for the error calculation and only the pressure drag C_{Dp} is taken into account for the error calculation. In the first case, the selector eliminates one input Tbl. 5.5 and in the second case, the selector eliminates four inputs Tbl. 5.6

5.2.3.4 Sub-design space Error

Three surrogate models were constructed, based on:

- All 24 design variables - original design space
- 15 design variables - design space after the Checker step
- 11 design variables - design space after the Selector step

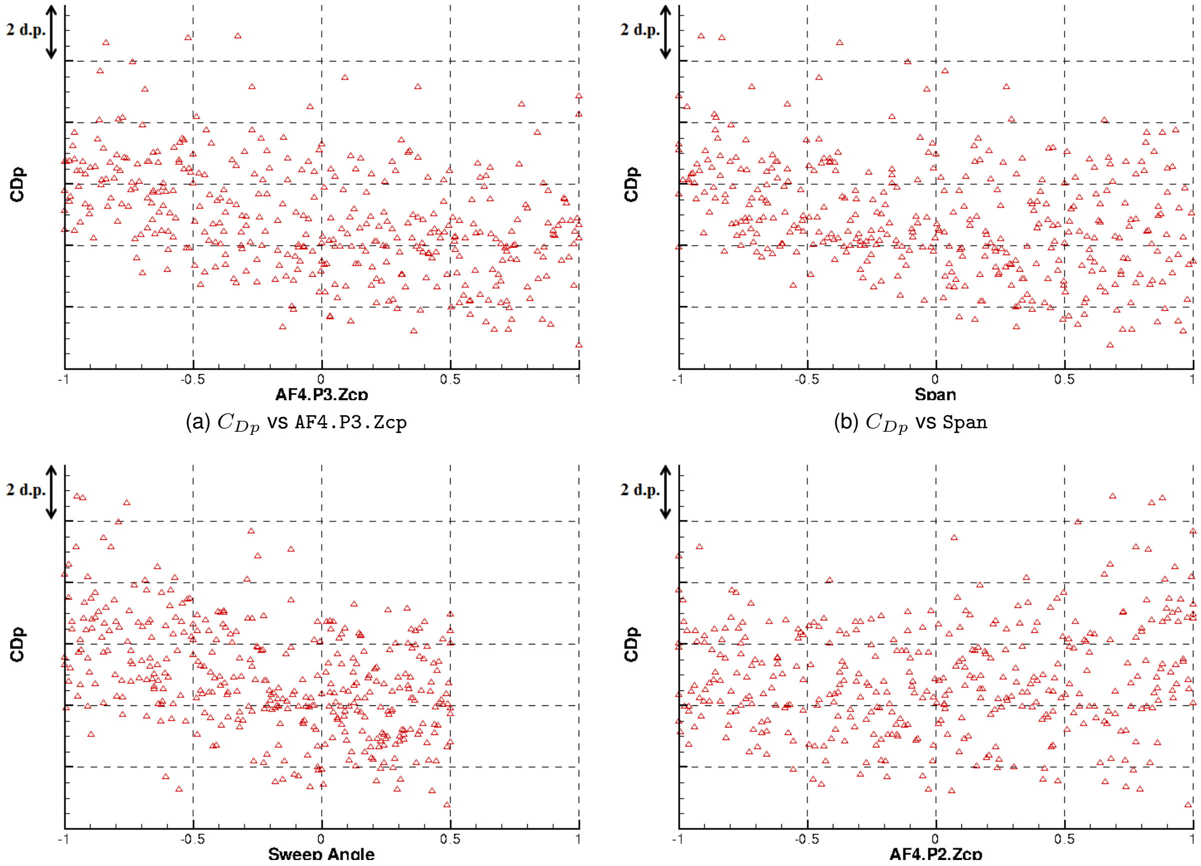

(a) C_{Dp} vs `AF4.P3.Zcp`

(b) C_{Dp} vs `Span`

(c) C_{Dp} vs `Sweep Angle`

(d) C_{Dp} vs `AF4.P2.Zcp`

Figure 5.8: C_{Dp} vs first four variables by Ranker

1	2	3	4	5
AF4.P3.Zcp	Span	Sweep Angle	AF4.P2.Zcp	AF4.P1.Zcp
6	7	8	9	10
AF5.P3.Zcp	AF5.P2.Zcp	AF5.P1.Zcp	AF4.Twist	AF5.Twist
11	12	13	14	15
A6.Twist	AF6.P3.Zcp	Height	AF7.Twist	AF8.P1.Zcp

Table 5.5: SDA Selector - Results (All-output error calculation)

1	2	3	4	5
AF4.P3.Zcp	Span	Sweep Angle	AF4.P2.Zcp	AF4.P1.Zcp
6	7	8	9	10
AF5.P3.Zcp	AF5.P2.Zcp	AF5.P1.Zcp	AF4.Twist	AF5.Twist
11	12	13	14	15
A6.Twist	AF6.P3.Zcp	Height	AF7.Twist	AF8.P1.Zcp

Table 5.6: SDA Selector - Results (C_{Dp} error calculation)

A plot of the mean and maximum errors is shown in Fig. 5.9. Both mean and maximum errors are minimized when the design space is reduced to 15 variables, corresponding to the subset given by the Checker. It seems that the nine variables eliminated by the Checker introduce statistical noise into the surrogate model, resulting in a higher error than with fifteen variables. The reduction to eleven variables is excessive - this is clearly supported by the fact that the Selector doesn't give the same result if the error is taken based on all outputs or C_{Dp} only - worsening surrogate model by losing information from the removed variables.

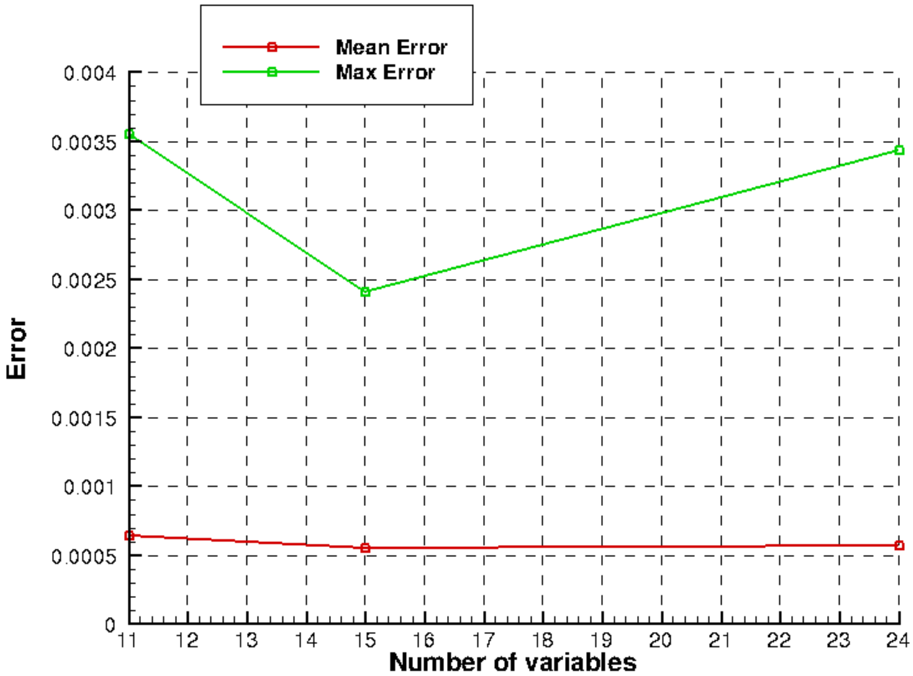

Figure 5.9: Sub-design space model error

These models can be used to optimize without the need of mesh deformation, CFD, adjoint state computation, etc. However, the optimized design must be verified using CFD analysis. On the other hand, adjoint CFD optimizations can be run with these subsets of design variables - although there is no gain in gradient computation time (adjoint method), it can possibly reduce the number of required evaluations, accelerating the optimization convergence speed.

5.3 Baseline Solution

The relevant aerodynamic coefficients at $C_{Lp} = 0.55$ are given in Tbl. 5.7. Furthermore, the position of the baseline design within the DOE cloud is given in Fig. 5.11.

C_{Lp}	C_{Df}/C_D^{nf}	C_{Dp}/C_D^{nf}
0.55122	22%	78%

Table 5.7: Baseline Winglet at $C_{Lp} = 0.55$

5.4 Adjoint Optimization

5.4.1 Starting from Baseline

5.4.1.1 Optimization Analysis

In order to solve Problem (5.1), an adjoint optimization is tried. The evolution of the objective function and constraint is shown Fig. 5.10a and the evolution of the KKT angle is plotted in Fig. 5.10b. The optimization clearly converges, with all iterations below the initial value. This is corroborated by the KKT angle that starts at around 148° and finishes at around 160°. The high starting value indicates that the baseline design is already relatively good. The final KKT angle value of 160° instead of the optimal 180° is explained by the optimization chain. One must not forget that many tools, each introducing its own error, are chained. Furthermore, the adjoint method is a first-order method, also introducing some error into the chain.

It is worth noting that the best design does not correspond to the last iteration. Neither does it correspond to the lowest values of objective function, since these might not satisfy the constraint. Indeed, the best designs correspond to iterations 15 and 17, both with an objective function value reduction of 1.4 drag points. The 15th design is however preferred, since it has a higher constraint margin and because it respects the KKT gradient condition slightly better. The position of the optimized design in the DOE cloud is shown in Fig. 5.11. It is well below the DOE envelope, meaning that the adjoint optimization starting from the baseline design achieves a better result than five hundred random designs.

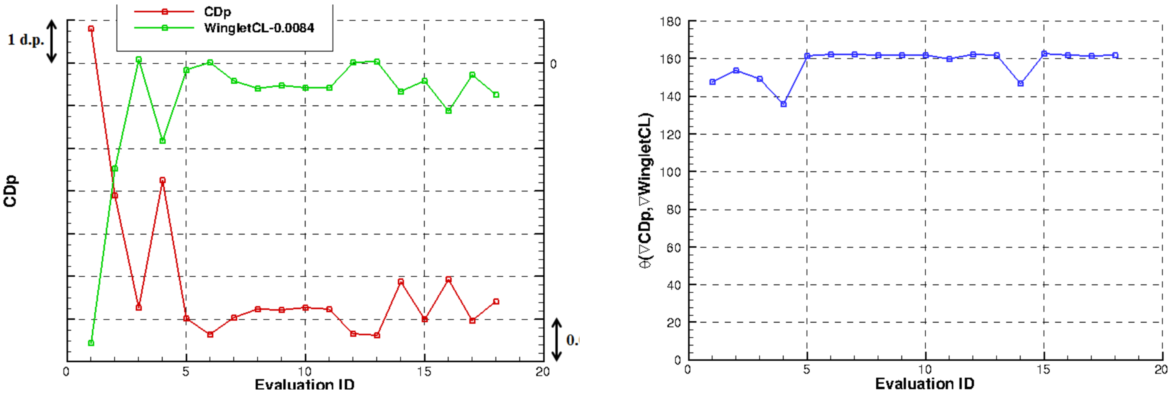

(a) Objective Function and Constraint

(b) KKT Angle

Figure 5.10: Optimization History - Initial Design: Baseline

5.4.1.2 Aerodynamic Analysis

Despite the fact that the optimization successfully reduced C_{Dp} by 1.4 drag points, the value of total drag C_D must be checked - although pressure drag has decreased, total drag might have increased due to an increase in friction drag. A far-field analysis drag decomposition presented in the form of a percentage variation with respect to the baseline design is given in Tbl. 5.8. Indeed, there is a gain in total drag C_D. However, it is smaller than the gain C_{Dp} because C_{Df} increased. The values of the

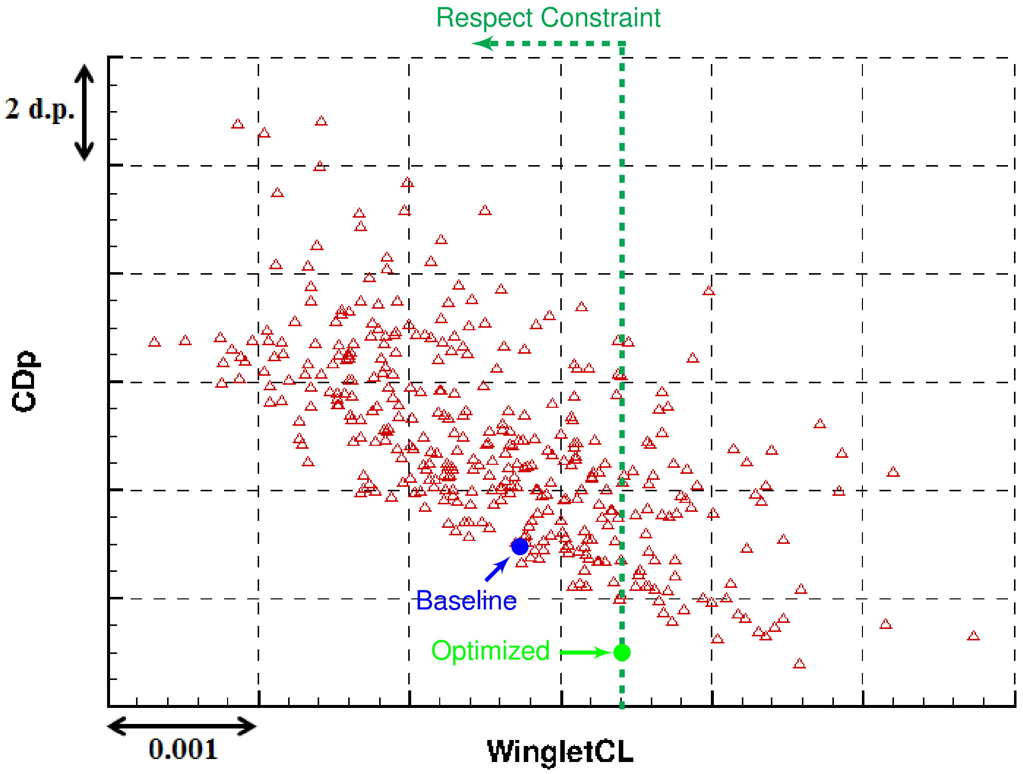

Figure 5.11: Baseline, Optimized - Position in C_{Dp} vs $(C_{Lp})_{\text{winglet}}$

design variables are presented in Tbl. 5.9, showing that `Span` was increased, which explains the increase in C_{Df}. Furthermore, both `Height` and `Sweep Angle` reach their maximum allowed values. This behavior is not very surprising, since increasing all these variables reduces C_{Dp}, as seen in Section 5.2.3. What is surprising is finding a combination of values that achieves a very good objective function value, while satisfying the constraint.

C_D^{nf}	C_{Df}	C_{Dp}	C_D^{ff}	C_{Dw}	C_{Dv}	C_{Di}	$-C_m$
-1.44	0.29	-1.73	-1.70	-0.16	1.10	-2.70	0.0016

Table 5.8: Optimized Winglet (starting from baseline) at $C_{Lp} = 0.550 \pm 0.001$ - Variation with respect to the baseline

5.4.2 Starting from DOE Designs

The adjoint optimization starting from the baseline design proved successful against all DOE designs. Yet, one might wonder if the baseline is the best design to start an adjoint optimization with. One strategy that might answer this question is chaining a DOE sample with an adjoint optimization. This way, a DOE is run, certain designs based on arbitrary criteria are selected and adjoint optimizations starting from these designs are run.

Three criteria were used to choose three candidates from the DOE pool:

<table>
<tr><th>Section</th><th>Twist</th><th>P1.Zcp</th><th>P2.Zcp</th><th>P3.Zcp</th></tr>
<tr><td><b>AF4</b></td><td>$+0.0076$</td><td>-0.1931</td><td>-0.0754</td><td>$+0.2610$</td></tr>
<tr><td><b>AF5</b></td><td>$+0.0544$</td><td>$+0.0811$</td><td>$+0.1818$</td><td>$+0.3712$</td></tr>
<tr><td><b>AF6</b></td><td>$+0.1009$</td><td>-0.0042</td><td>$+0.0753$</td><td>$+0.3368$</td></tr>
<tr><td><b>AF7</b></td><td>$+0.1282$</td><td>$+0.0707$</td><td>$+0.0478$</td><td>$+0.2119$</td></tr>
<tr><td><b>AF8</b></td><td>$+0.0047$</td><td>$+0.0074$</td><td>$+0.0005$</td><td>$+0.0051$</td></tr>
<tr><td><b>Span</b></td><td colspan="4">$+0.7098$</td></tr>
<tr><td><b>Height</b></td><td colspan="4">$+0.9996$</td></tr>
<tr><td><b>Sweep Angle</b></td><td colspan="4">$+0.5000$</td></tr>
<tr><td><b>Taper Ratio</b></td><td colspan="4">-0.0016</td></tr>
</table>

Table 5.9: Optimum design variables

1. Best (objective function-wise) of all candidate designs
2. Best (objective function-wise) of all candidate designs that respect the constraint
3. Good (objective function-wise) candidate with a high margin with respect to the problem constraint

These candidates will be called DOE$\mathtt{x}$, where $\mathtt{x}$ is their number on the previous list.

5.4.2.1 Optimization Analysis

The evolution of the objective function, constraint and KKT angle is shown Fig. 5.12. All optimizations converge and the KKT angle final value is around 160° for all except DOE3, which achieves 170°. Once again, it is worth noting that the best designs do not necessarily correspond to the last iteration. The optimums are found at iteration 15, 16, 11, 10, for the baseline, DOE1, DOE2 and DOE3 optimizations, respectively. All designs that do not respect the constraint, even by a very small value, are not considered.

5.4.2.2 Aerodynamic Analysis

A far-field drag decomposition is shown in Tbl. 5.8 for the optimized designs. They all present very close values of ΔC_D^{nf}, with the DOE3 optimized design being the best. The difference is however very small and within the error margin. Fig. 5.13 presents the C_p distribution on the upper and lower sides of the winglet, for the following designs: baseline, optimized from baseline and optimized from DOE3. It can be seen that the new winglet designs act by reducing suction on the upper side near the wingtip. On the lower side, the strongest pressure zone (yellow zone) is also smaller.

5.5 Optimized Database

Varying all parameters in the DOE is cumbersome, since the number of dimensions of the design space is 24. Instead of running the DOE on all parameters, a subset can be chosen and adjoint optimizations

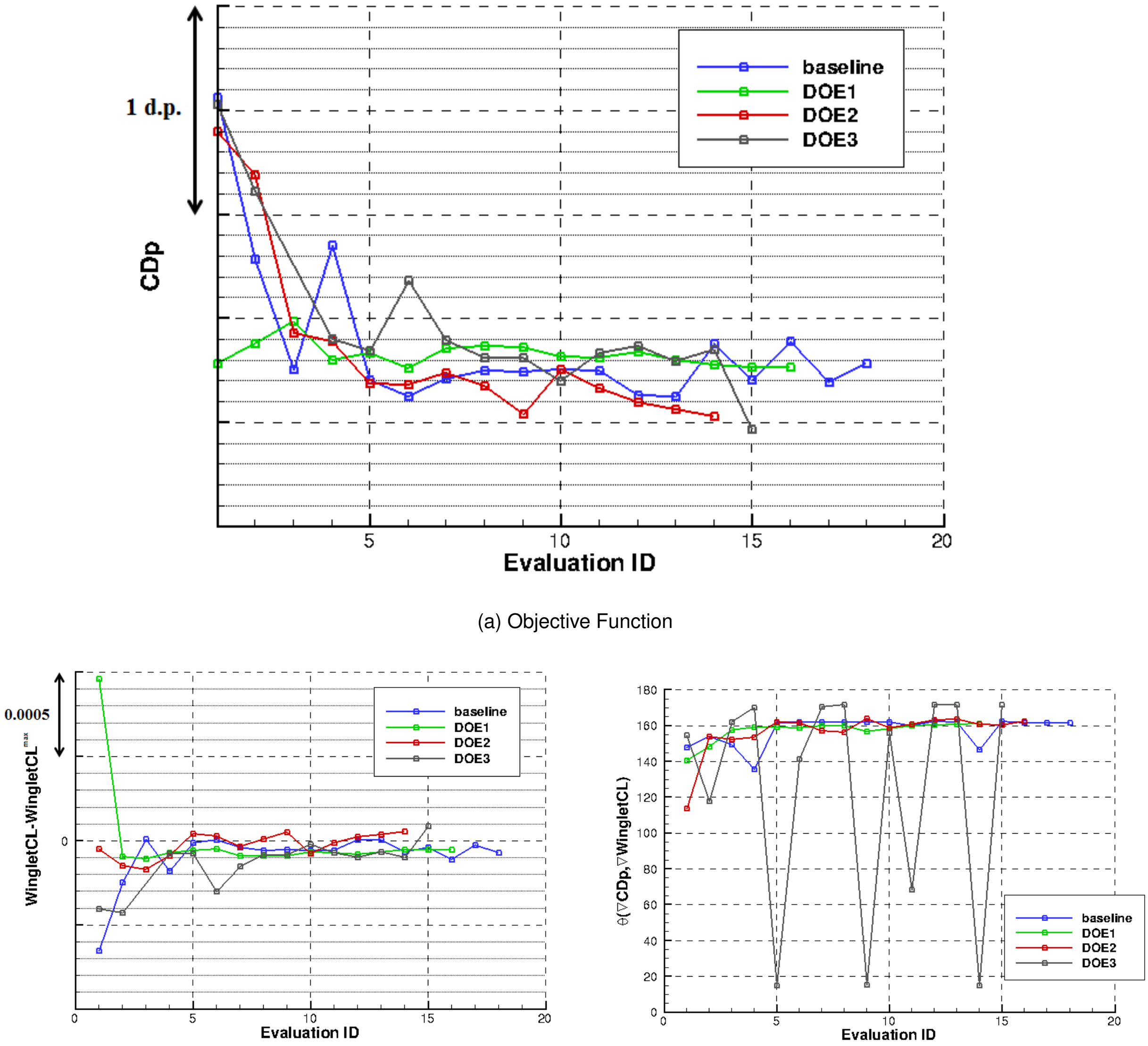

(a) Objective Function

(b) Constraint

(c) KKT Angle

Figure 5.12: Optimization History - Initial Design: Baseline, DOE1, DOE2, DOE3

	C_D^{nf}	C_{Df}	C_{Dp}	C_D^{ff}	C_{Dw}	C_{Dv}	C_{Di}	$-C_m$
Opt. Base	-1.44	0.29	-1.73	-1.70	-0.16	1.10	-2.70	0.0016
Opt. DOE1	-1.43	0.24	-1.67	-1.60	-0.16	1.00	-2.50	0.0016
Opt. DOE2	-1.43	0.34	-1.77	-1.90	-0.15	1.40	-3.13	0.0018
Opt. DOE3	-1.50	0.24	-1.74	-1.60	-0.14	1.00	-2.50	0.0016

Table 5.10: Optimized Winglets at $C_{Lp} = 0.550 \pm 0.001$ - Variation with respect to the baseline

can be run using the rest of the parameters. Another advantage to this strategy is that it generates an optimized design database that can be afterwards used, for example, for mathematical optimizations.

The natural separation of the design space is planform parameters and twist and camber parameters. The DOE generates designs using the four planform parameters, while twist and camber parameters re-

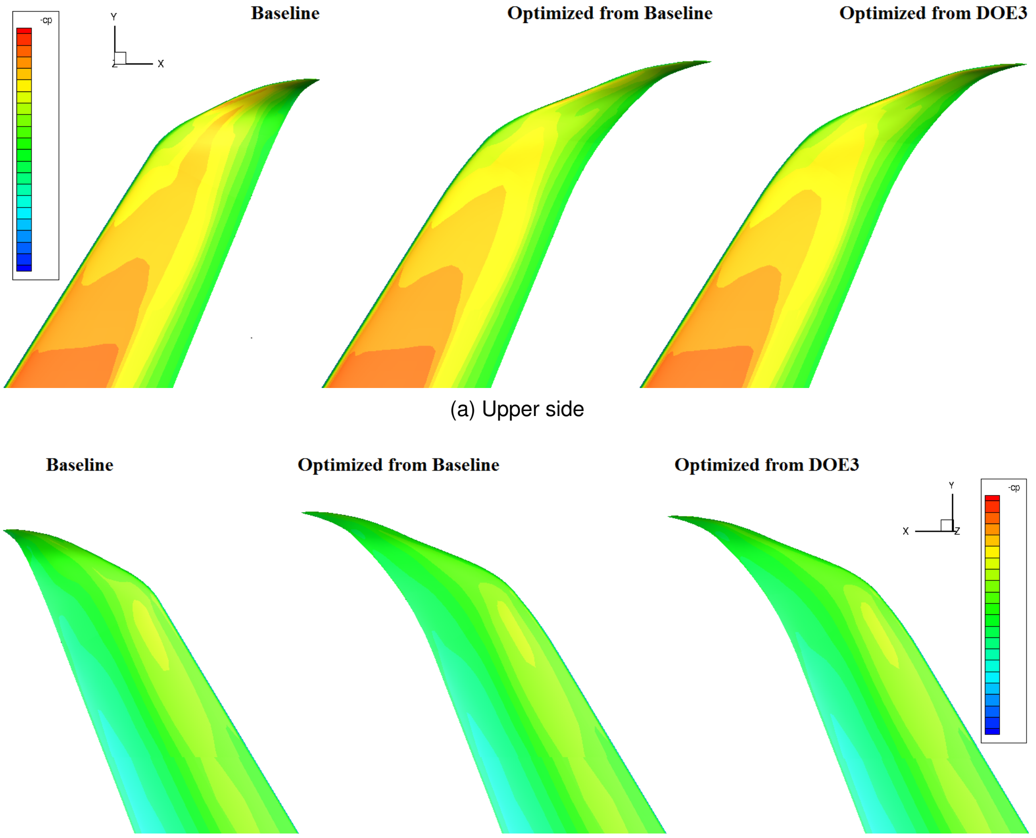

(a) Upper side

(b) Lower side

Figure 5.13: C_p distribution on winglet

main constant at their baseline value 0. Then, an adjoint optimizations is run starting on each generated design. This time though, the planform parameters are locked to their DOE values and the design variables are the camber and twist parameters.

5.5.1 Planform DOE

The DOE is run on the four planform variables: span, height, sweep angle and taper ratio. The sampling algorithm is the Latin Hypercube Sampling and a total of fifty samples were generated. In fact, the 50-sample DOE was run many times with the objective of maximizing the minimum and average distance between samples. Fig. 5.14 plots the generated data points in two plans for the chosen DOE.

5.5.2 Optimized Solutions

Fig. 5.15 shows both the original (pre-optimization) and final (post-optimization) C_{Dp} and constraint values, as well as the corresponding C_{Dp} gains. There is an evident anti-correlation between C_{Dp} and Span Fig. 5.15a. As Span increases, the pressure drag gain decreases, becoming a loss instead of a gain beyond a certain point. This behavior is related to the initial constraint value, which can be seen in Fig. 5.15b: as Span increases, there is less margin for the adjoint optimizer to work with; for very high values of Span, the constraint is not respected, which is fixed by the optimizer at the expense of the objective function. A Span increase results in a bigger lifting surface that generates more lift, on which

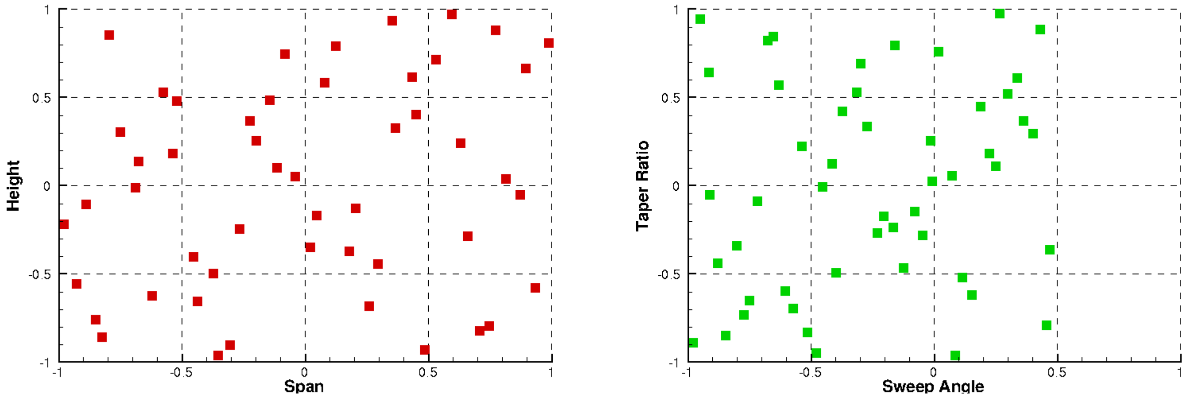

(a) Height vs Span

(b) Taper Ratio vs Sweep Angle

Figure 5.14: Planform DOE - 50 samples

the constraint imposes a limit. C_{Dp} is also anti-correlated with Height. However, this anti-correlation is much weaker than in the previous case. Furthermore, the pressure drag gain is uniformly distributed, as well as the initial constraint value. Sweep Angle presents the stronger anti-correlation with C_{Dp} of all four planform variables. However and contrarily to Span, the gain obtained by retwisting and recambering is not dependent on Sweep Angle, which is a direct consequence of the fact that Sweep Angle does not influence the constraint. Taper is the least interesting of these parameters. There is no variable with a particular dependence on it, confirming the sensitivity analysis in Section 5.2.3.

Finally, three designs are seen to be close to a 1.4 gain of C_{Dp}. However, their C_{Dp} values are slightly higher than the previous optimized designs'.

5.6 Conclusion

This problem involved the redesign of the winglet of long range airliner designed by Airbus. This redesign was limited to changes in planform, retwist and recamber, while the objective was to minimize drag pressure, under a maximum load constraint.

Since the winglet is a complex shape, which forcibly results in complex aerodynamics, the behavior of the design space is not trivial. To understand it and to assess the importance of each design variable, a DOE was run on all parameters. The results of which were then analyzed, drawing important conclusions, such as the link between objective function and constraint, explicitly demonstrating that the maximum load constraint could not be removed. Furthermore, a sensitivity and dependency analysis was executed based on the designs generated by the DOE. This analysis allowed the determination of design variables that don't have correlation with any of the outputs and supplied a ranking of the remaining variables according to their individual importance.

An adjoint optimization was run starting from the baseline design, resulting in a considerable reduction of 1.4 drag points. The optimized design validated the previous analysis on the importance of each design variable - the most relevant variables were at (or near) their extreme values.

Although starting an adjoint optimization from the baseline design resulted in a good C_{dp} reduction,

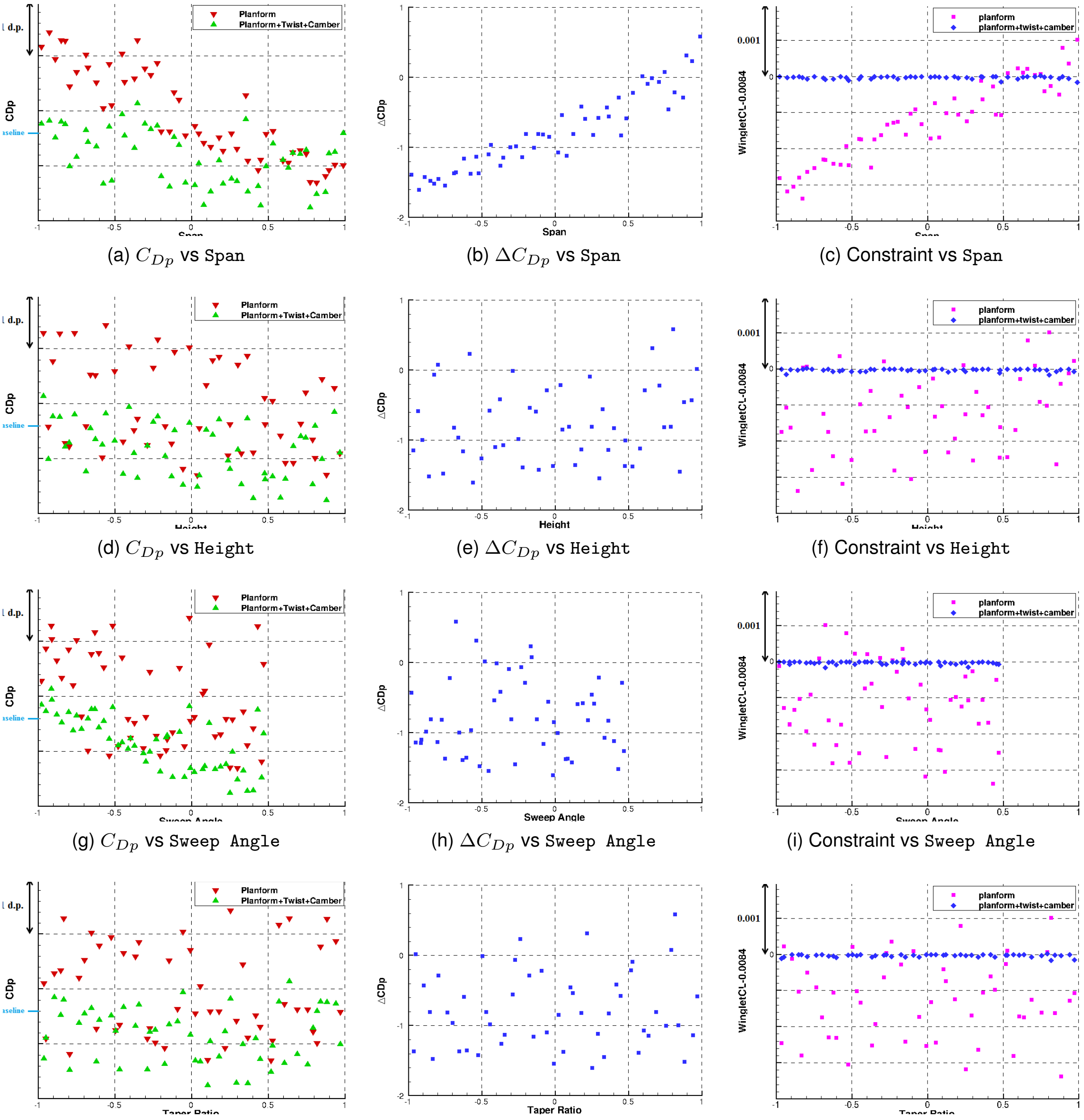

(a) C_{Dp} vs `Span`

(b) ΔC_{Dp} vs `Span`

(c) Constraint vs `Span`

(d) C_{Dp} vs `Height`

(e) ΔC_{Dp} vs `Height`

(f) Constraint vs `Height`

(g) C_{Dp} vs `Sweep Angle`

(h) ΔC_{Dp} vs `Sweep Angle`

(i) Constraint vs `Sweep Angle`

(j) C_{Dp} vs `Taper`

(k) ΔC_{Dp} vs `Taper`

(l) Constraint vs `Taper`

Figure 5.15: `Planform` vs `Planform+Twist+Camber` - C_{Dp}, ΔC_{Dp}, Constraint

is it possible that other points might result in an even better reduction? To answer this, three seed designs from the DOE database were selected, according to pertinent criteria. The optimizations starting from the three seed designs were run. All optimizations resulted in very similar values to the baseline optimization, with the third optimized being slightly better, but within error margin.

Finally, it is argued that a DOE on all parameters may not be the best way to explore the design space and optimize. The high number of dimensions of the design space requires too many samples. The proposed solution was to run the DOE on the planform parameters, with twist and camber frozen at the baseline value 0 and then optimize the generated designs with twist and camber parameters, while the planform parameters are frozen at their DOE values. The generated optimized database confirms the results from the sensitivity and dependency analysis and from the previous optimizations. This strategy didn't produce the best design, though it did generate designs whose performances are close to that of the previous optimized designs.

Globally, the robustness of the adjoint optimization method for the current case was demonstrated. In cases where the starting design does not respect the constraint, the optimizer successfully produces a design that respects the constraint at the expense of the objective function. In cases where the starting design did respect the constraint, the design was successively driven towards the boundary of the constraint, which is in agreement with the optimality conditions. Furthermore, the adjoint optimization alone starting from the baseline design produced a solution of the same or better quality than most of the optimized designs obtained by chaining a DOE with an adjoint optimization.

Chapter 6

Conclusion

The developed work was centered around the subject of aerodynamic optimization in an industrial context. More specifically, multiple strategies based on the adjoint method for gradient computation were employed in two test cases: two-dimensional transonic airfoil and winglet of a long range Airbus aircraft. The merits and robustness of the gradient-based optimization with gradient computed by the adjoint method were demonstrated:

- The optimizations converged to better designs (in terms of objective function) that satisfy (to some error margin) the problem's optimality conditions.
- The optimization process handled well both equality and inequality constraints

Regarding the two-dimensional case, the optimization problem was defined and an unconstrained optimization was run to solve it. The resulting design improved the objective function. However, it didn't have the desired global behavior, since it shifted the maximum of $\frac{C_{lp}}{C_d}$ to a higher value of C_{lp} . This was fixed by adding a constraint to the optimization problem. This constrained optimization also achieved an improvement of the objective function of 3.60%, though smaller than the unconstrained optimization one. Nevertheless, it showed the desired global behavior of maintaining the maximum of $\frac{C_{lp}}{C_d}$ at the baseline's maximum location of $C_{lp} = 0.63$. Finally, it was shown that the location of the maximum of $\frac{C_{lp}}{C_d}$ could willingly be changed to a desired value of $C_{lp} = C_{lp}^{*} < 0.63$ at the expense $\frac{C_{lp}}{C_d}$.

Based on the knowledge acquired from the two-dimensional case, focus was shifted to the three-dimensional case of the long range airliner winglet. Here, there is an increase of complexity in shape and aerodynamics, especially highlighted by the difficulty of predicting the performance behavior with respect to the design variables, apart from particular cases. In order to address this problem, the DOE technique was introduced and executed. It rendered possible an analysis of sensitivity and dependency. This analysis allowed the determination of design variables that don't have correlation with any of the outputs and supplied a ranking of the remaining variables according to their individual importance. Multiple strategies were employed: pure adjoint optimization starting from the baseline design and adjoint optimization starting from three DOE designs. All four optimizations converged, resulting in very close values, demonstrating the effectiveness of the adjoint optimization alone as a sufficient optimization process. The hybrid strategy of chaining a DOE with adjoints optimizations was reformulated. This time, the DOE only changed the planform, while the adjoint optimization only worked with twist and camber parameters. This strategy didn't produce the best design, though it did generate designs whose performances are close to that of the previous optimized designs.

Aerodynamic optimization methods, within an industrial framework such as Airbus, were employed with success to the optimization of real-life cases. Moreover, results which are not trivial were found and important conclusions drawn upon. Aerodynamic optimization is a relatively young subject and Airbus demonstrates its presence in the front edge of this discipline.

6.1 Future Work

The two-dimensional study could be redone with another parameterization, for example, by adding another point of control to the camber line. Furthermore, instead of an equality constraint, an inequality constraint, such as $|f_{\text{left}} - f_{\text{right}}| \leq \epsilon$ allowing a tolerance ϵ could be introduced. This could potentially ease the task of the optimizer since the constraint is not as strict as before, while still achieving the desired result.

The three-dimensional study produced some interesting possibilities that were not studied due to the extensiveness of the work, such as: mathematical optimization on surrogate models with CFD validation and adjoint optimization on the reduced subset of variables. It would be extremely important if it were verified, for example, that the surrogate models perform as well as (or better than) the adjoint optimizations.

Bibliography

[1] IATA. Economic performance of the airline industry. Report, June 2014.

[2] A. Jameson, N. A. Pierce, and L. Martinelli. Optimum aerodynamic design using the Navier–Stokes equations. In *Theoretical and Computational Fluid Dynamics*, volume 10, pages 213–237. Springer-Verlag GmbH, Jan. 1998.

[3] J. J. Reuther, A. Jameson, J. J. Alonso, M. J. RimlInger, and D. Saunders. Constrained multi-point aerodynamic shape optimization using an adjoint formulation and parallel computers, part 2. *Journal of aircraft*, 36(1):61–74, 1999.

[4] A. Jameson. Aerodynamic shape optimization using the adjoint method. *Lectures at the Von Karman Institute, Brussels*, 2003.

[5] S. Nadarajah and A. Jameson. Studies of the continuous and discrete adjoint approaches to viscous automatic aerodynamic shape optimization. *AIAA paper*, 2530:2001, 2001.

[6] M. O. Branch. Aerodynamic shape optimization based on free-form deformation. 2004.

[7] J. Brezillon and N. Gauger. 2d and 3d aerodynamic shape optimisation using the adjoint approach. *Aerospace Science and Technology*, 8(8):715–727, 2004.

[8] A. Dumont, A. Le Pape, J. Peter, and S. Huberson. Aerodynamic shape optimization of hovering rotors using a discrete adjoint of the reynolds-averaged navier–stokes equations. *Journal of the American Helicopter Society*, 56(3):1–11, 2011.

[9] J. Brezillon and R. P. Dwight. Applications of a discrete viscous adjoint method for aerodynamic shape optimisation of 3d configurations. *CEAS Aeronautical Journal*, 3(1):25–34, 2012.

[10] A. Bueno-Orovio, C. Castro, F. Palacios, and E. Zuazua. Continuous adjoint approach for the spalart-allmaras model in aerodynamic optimization. *AIAA journal*, 50(3):631–646, 2012.

[11] R. P. Dwight and J. Brezillon. Effect of approximations of the discrete adjoint on gradient-based optimization. *AIAA journal*, 44(12):3022–3031, 2006.

[12] J. Brezillon and R. P. Dwight. Aerodynamic shape optimization using the discrete adjoint of the navier-stokes equations: applications towards complex 3d configurations. In *Proceedings of the CEAS/KATnet Conference on Key Aerodynamic Technologies, 12-14 May 2009, Bremen, Germany*, 2009.

[13] G. Carrier, D. Destarac, A. Dumont, M. Méheut, I. Din, J. Peter, S. B. Khelil, J. Brezillon, and M. Pestana. Gradient-based aerodynamic optimization with the elsa software. In *52nd Aerospace Sciences Meeting*, pages 2014–0568, 2014.

[14] T. M. Leung and D. W. Zingg. Aerodynamic shape optimization of wings using a parallel newton-krylov approach. *AIAA journal*, 50(3):540–550, 2012.

[15] Z. Lyu and J. R. Martins. Aerodynamic design optimization studies of a blended-wing-body aircraft. *Journal of Aircraft*, 51(5):1604–1617, 2014.

[16] Z. Lyu, G. K. Kenway, and J. Martins. Rans-based aerodynamic shape optimization investigations of the common research model wing. In *AIAA Science and Technology Forum and Exposition (SciTech), National Harbor, MD*, 2014.

[17] I. Ghazlane, G. Carrier, A. Dumont, and J. Desideri. Aerostructural adjoint method for flexible wing optimization. *AIAA Paper*, 1924:2012, 2012.

[18] D. Kraft. A software package for sequential quadratic programming. *Tech. Rep. DFVLR-FB*, 88(28), 1985.

[19] P. R. Spalart and S. R. Allmaras. A one-equation turbulence model for aerodynamic flows. *Recherche Aerospatiale*, (1):5–21, 1994.

[20] S. Catris and B. Aupoix. Density corrections for turbulence models. *Aerospace Science and Technology*, 4:1–11, 2000.

[21] V. de Brederode. *Fundamentos de Aerodinâmica Incompressível*. IDMEC, 1^{st} edition, 1997. ISBN:972-97402-0-8.

[22] D. Destarac and J. van der Vooren. Drag/thrust analysis of jet-propelled transonic transport aircraft: Definition of physical drag components. *Aerospace Science and Technology*, 8(6):545–556, 2004. doi:10.1016/j.ast.2004.03.004.

[23] E. J. Nielsen and M. A. Park. Using an adjoint approach to eliminate mesh sensitivities in computational design. *AIAA journal*, 44(5):948–953, 2006.

[24] DATADVANCE. Macros, 2015. URL `https://www.datadvance.net/product/macros/manual/5.2/index.html`.